Deficiency of Heterogeneous Nuclear Ribonucleoprotein U leads to delayed neurogenesis

Francesca Mastropasqua[1,2], Marika Oksanen[1,2], Cristina Soldini[1,2], Shemim Alatar[1,2], Abishek Arora[1,2], Roberto Ballarino[3,4,5], Maya Molinari[6], Federico Agostini[4,5], Axel Poulet[7], Michelle Watts[1,2], Ielyzaveta Rabkina[1,2], Martin Becker[1,2], Danyang Li[1,2], Britt-Marie Anderlid[8,9], Johan Isaksson[1,10], Karl Lundin Remnelius[1], Mohsen Moslem[6], Yannick Jacob[7], Anna Falk[6,11], Nicola Crosetto[3,4,12], Magda Bienko[3,4,12], Emanuela Santini[6], Anders Borgkvist[6], Sven Bölte[1,2,13,14] and Kristiina Tammimies[1,2*]

[1]Center of Neurodevelopmental Disorders (KIND), Centre for Psychiatry Research, Department of Women's and Children's Health, Karolinska Institute, Region Stockholm, Stockholm, Sweden.

[2]Astrid Lindgren Children's Hospital, Karolinska University Hospital, Region Stockholm, Stockholm, Sweden

[3]Department of Microbiology, Tumor and Cell Biology, Karolinska Institutet, Stockholm, Sweden

[4]Science for Life Laboratory, Tomtebodavägen 23A, Solna, Sweden

[5]Department of Medical Biochemistry and Biophysics, Karolinska Institutet, Stockholm, Sweden.

[6]Department of Neuroscience, Karolinska Institutet, Solna, Sweden

[7]Department of Molecular, Cellular and Developmental Biology, Yale University, New Haven, CT, USA

[8]Department of Molecular Medicine and Surgery, Karolinska Institutet, Stockholm, Sweden

[9]Department of Clinical Genetics, Karolinska University Hospital, Stockholm, Sweden

[10]Department of Medical Sciences, Child and Adolescent Psychiatry Unit, Uppsala University, Uppsala, Sweden

[11]Lund Stem Cell Center, Lund University, Lund, Sweden

[12]Human Technopole, Viale Rita Levi-Montalcini 1, 20157 Milan, Italy

[13]Curtin Autism Research Group, Curtin School of Allied Health, Curtin University, Perth, Western Australia

[14]Child and Adolescent Psychiatry, Stockholm Health Care Services, Region Stockholm, Stockholm, Sweden.

[*]Correspondence: kristiina.tammimies@ki.se

Corresponding Author:

Kristiina Tammimies, PhD

Postal address: BioClinicum J9:30, Visionsgatan 4, 171 56 Solna, Sweden

E-mail: kristiina.tammimies@ki.se

Summary

Genetic variants affecting *Heterogeneous Nuclear Ribonucleoprotein U (HNRNPU)* have been identified in several neurodevelopmental disorders (NDDs); however, the role of *HNRNPU* in human neural development and NDDs remains to be studied. Here, we describe the molecular and cellular outcomes of *HNRNPU* deficiency during *in vitro* neural differentiation of isogenic and patient-derived neuroepithelial stem cells. We demonstrate that *HNRNPU* deficiency leads to chromatin remodeling of A/B compartments, and transcriptional rewiring, partly by impacting exon inclusion during mRNA processing. Genomic regions affected by the chromatin restructuring and host genes of exon usage differences show a strong enrichment for genes implicated in epilepsies, intellectual disability, and autism. Lastly, we show the effects of the molecular reorganization at the cellular level, where *HNRNPU* downregulation leads to altered neurogenesis and an increased fraction of neural progenitors marked in the maturing neuronal population. We conclude that *HNRNPU* deficiency is responsible for the delayed commitment of neural progenitors to neuronal maturation, ultimately leading to altered neurogenesis.

INTRODUCTION

Enormous progress in genomic technologies has led to the discovery of hundreds of genes associated with various neurodevelopmental disorders (NDDs). These include several genes belonging to the heterogeneous nuclear ribonucleoprotein (hnRNP) family (Gillentine et al., 2021). One of the genes within this family, *HNRNPU*, which encodes for Heterogeneous Nuclear Ribonucleoprotein U (also known as Scaffold Attachment Factor A (SAF-A)) (Kiledjian and Dreyfuss, 1992), has emerged as a frequently affected gene leading to NDDs such as intellectual disability (ID), autism spectrum disorder (ASD) as well as neurological conditions such as epilepsies (Depienne et al., 2017; Satterstrom et al., 2020; Taylor et al., 2022). The pathogenic genetic variants affecting the *HNRNPU* gene in individuals with *HNRNPU*-related disorder are mostly *de novo* loss-of-function variants at sequence or copy number level (Brunet et al., 2021; Durkin et al., 2020; Gillentine et al., 2021; Wang et al., 2020). All the reported cases are heterozygous variants, suggesting that homozygous gene-disrupting variants affecting *HNRNPU* are embryonic lethal in humans, similar to what has been demonstrated in mice (Dugger et al., 2020; Roshon and Ruley, 2005; Ye et al., 2015).

HNRNPU has a key role in 3D genome organization and regulating RNA processing (Fan et al., 2018; Marenda et al., 2022; Nozawa et al., 2017; Xiong et al., 2020; Ye et al., 2015). For instance, HNRNPU modulates chromatin compaction by promoting chromatin accessibility in a dynamic yet structured fashion, dependent on its oligomerization status (Nozawa et al., 2017). Recent studies have also shown the involvement of HNRNPU in mitosis and cell division by changing its interactions with condensed chromatin and influencing DNA replication and sister chromatid separation (Connolly et al., 2022; Ma et al., 2011; Sharp et al., 2020). Several studies have reported a role for HNRNPU in splicing, promoting both exon inclusion and exclusion (Huelga et al., 2012; Jones et al., 2022; Ye et al., 2015). Mechanistically, it has been shown that HNRNPU can stabilize the pre-mRNA structure, thus inhibiting the splicing of certain exons (Jones et al., 2022). A critical role for Hnrnpu mediated splicing has also been demonstrated during pre- and postnatal heart development in mice, showing that loss of *Hnrnpu* leads to increased intron retention events, causing abnormality in heart development and function (Ye et al., 2015).

The majority of functional studies investigating the role of HNRNPU have been conducted in non-brain cell lines or tissues. However, a mouse model of *Hnrnpu* haploinsufficiency was recently described, characterized by abnormal brain organization and an altered transcriptome with downregulation of pathways related to neuronal projection and migration and upregulation of genes relevant to cell growth and protein localization (Dugger et al., 2020). In contrast, another study showed upregulation of genes involved in synaptic activity and downregulation of DNA-related ontologies together with changes in alternative splicing regulation upon complete conditional *Hnrnpu* knockout in the mouse brain (Sapir et al., 2022). Therefore, gene dosage might be a determining factor in the overall outcome of *HNRNPU* genetic variants. Nonetheless, the effects of heterozygous *HNRNPU* loss-of-function variants during physiologic human neural development have not yet been studied. Therefore, we aim to delineate the molecular and cellular consequences of *HNRNPU* deficiency in human induced pluripotent stem cell (iPSC)-derived models of early neural development.

RESULTS

Generation and characterization of *HNRNPU* knockdown in iPS and neuroepithelial stem cells

To assess the molecular effects of *HNRNPU* haploinsufficiency during human neural differentiation, we generated two different *HNRNPU* deficient cellular models derived from human iPSCs. The iPSCs were induced into neuroepithelial stem (NES) cells and further differentiated for 5 (D5) and 28 (D28) days using an undirected protocol as previously described (Becker et al., 2020; Falk et al., 2012) (**Figure 1A**). This approach generates a neuronal culture consisting of a mixed population of excitatory, inhibitory, and progenitor cells representing a physiological neuronal environment.

We first generated an isogenic cell model, hereafter called siHNRNPU, in which we reduced HNRNPU protein expression by 32% using a pool of small interfering RNA (siRNA) oligos in NES cells obtained from a neurotypical control (CTRL) male (Uhlin et al., 2017a) in parallel with non-target oligo pool (siNTC), similar to approaches successfully used in previous studies of HNRNPU in other cell types (Ma et al., 2011; Nozawa et al., 2017; Zietzer et al., 2020) (**Figure S1A**). To achieve sufficient knockdown of HNRNPU protein throughout differentiation, we performed repetitive siRNA treatments every six days, reducing the protein levels to 29% at D28 compared with siNTC samples (**Figure S1B**).

As a complementary approach, we generated an *HNRNPU*-related disorder patient cell model. Through genetic screening of a twin cohort focusing on NDDs, we identified a male twin pair carrying a 44 kilobase (kb) heterozygous deletion spanning from *COX20* to *HNRNPU* genes (Stamouli et al., 2018). The twins were diagnosed with ASD, ID, and fever-induced seizures. A detailed phenotypic description of the twin pair is presented in **Supplementary Table 1**. We obtained fibroblasts from skin biopsies of the twins and successfully reprogrammed twin-2 fibroblasts into iPSCs (hereafter called $HNRNPU_{del/+}$). The iPSCs had a normal karyotype and pluripotent marker expression (**Figure S1C and S1D**). In addition, we used dual-SMAD inhibition to derive NES cells from the $HNRNPU_{del/+}$ iPSCs as previously described (Falk et al., 2012), followed by staining for neuronal stem cell markers Nestin and SRY (sex determining region Y)-box 2 (SOX2) to verify their identity (**Figure S1E**). To confirm the downregulation of HNRNPU, we measured *HNRNPU* RNA and protein in $HNRNPU_{del/+}$ cells using CTRL cells as a reference. $HNRNPU_{del/+}$ showed significantly lower RNA expression ($P < 1.0\text{x}10^{-5}$, ANOVA and posthoc

Tukey test) and an average lower expression of HNRNPU protein but with high variability (**Figure 1B and Figure S1F**). Our results of the variable protein expression are consistent with a recent report showing that downregulation of *HNRNPU* at the RNA level does not translate into a similar reduction at the protein level due to compensatory mechanisms (Dugger et al., 2020; Sapir et al., 2022).

HNRNPU expression changes during neural differentiation and brain development

Next, we sought to analyze the molecular consequences of *HNRNPU* haploinsufficiency during human neural development. To this end, we extracted total RNA for transcriptomic analyses from NES cells collected at three different time points of differentiation (D0, D5, and D28). In the CTRL cell line, *HNRNPU* expression decreased steadily during differentiation (comparison D0-D5: P = 0.019; D5-D28: P = < 1.0×10^{-5}, ANOVA and posthoc Tukey test), similar to what was observed in all the cerebral areas during brain development and during differentiation from iPSCs to neurons from a previously published dataset (Burke et al., 2020) (**Figure 1B-D**). Since *HNRNPU* expression was higher in proliferating progenitor cells (**Figure 1B** and Sapir et al., 2022), we further inspected its expression in CTRL cells at D28 using our previously published single-cell RNA sequencing data from D28 neural culture (Becker et al., 2020) (**Figure S1G**). As expected, *HNRNPU* expression was highest in the neural progenitor cluster (**Figure S1H-I**). Moreover, the neural progenitor cluster was further divided into three distinct subclusters, of which one was highly enriched in proliferating markers such as *TOP2A*, *KIFC1,* and *KIF18B.* This cluster also had the highest expression of *HNRNPU* (**Figure S1J**).

In contrast to CTRL cells, the expression of *HNRNPU* in $HNRNPU_{del/+}$ cells was stable from D0 to D5 (P = 0.99, ANOVA and posthoc Tukey test), followed by a significantly delayed decrease at D28 (D5-D28, P = 2.6×10^{-5}, ANOVA and posthoc Tukey test) (**Figure 1B**). At D0 and D5, *HNRNPU* expression was significantly lower in $HNRNPU_{del/+}$ cells compared with CTRL cells (P < 1.0×10^{-5} and 2.3 $\times 10^{-5}$, respectively, ANOVA and posthoc Tukey test), while the expression was similar between the two cell lines at D28 (P = 0.58, ANOVA and posthoc Tukey test) (**Figure 1B**). HNRNPU protein was predominantly localized in the nucleus at all three analyzed stages of differentiation, and the measured protein levels were extremely variable between different time points in both cell lines and did not mirror mRNA levels (**Figure S2A-B**). These results show that physiologically *HNRNPU* has the highest expression in the neuroepithelial

stem cell stage and steadily reduces during the differentiation demonstrating its important role in early neural differentiation.

HNRNPU expression impacts cell differentiation pathways

Next, we performed differential gene expression analyses using DESeq2 (Love et al., 2014), followed by gene set enrichment analysis (GSEA) of the obtained transcriptomic data. Similar to earlier reported results in other cell types (Nozawa et al., 2017), we found that *HNRNPU* downregulation had a limited effect on the transcriptional landscape at D0 and D5. The isogenic siHNRNPU cells (replicates n=5) had only 10 differentially expressed genes (DEG) at D0 and 30 DEG at D5 (Base Mean> 20, |log2FoldChange| > 0.58, *P* adjusted < 0.05, Wald test and Benjamini-Hochberg procedure) (**Supplementary Table 2A-B**). As expected, due to the different genetic backgrounds, when comparing $HNRNPU_{del/+}$ cells (replicates n=5) to the CTRL cell line (replicates n=5) at each time point, we identified a higher number of DEG (2091 DEG at D0 of which 1033 upregulated and 1058 downregulated; 2091 DEG at D5, of which 1251 upregulated and 840 downregulated genes) (**Supplementary Table 2C-D**). At D28 of the neural differentiation, both *HNRNPU*-deficient models showed wider transcriptional rewiring, with 1511 DEG in siHNRNPU and 1608 DEG in $HNRNPU_{del/+}$ cells (**Supplementary Table 2E-F**). Of these, only 148 DEG genes were shared between the two models at D28, suggesting that downregulation of *HNRNPU* might affect the expression of upstream transcriptional regulators that increase the transcriptomic landscape variability.

Next, we analyzed gene set and pathway level changes across the two datasets (**Supplementary Table 3**). At D0, no specific Gene Ontology (GO) terms or enriched pathways were significantly shared between the two models (**Figure 2A, Figure S3A, and Supplementary Table 3A-D**). At D5, genes affecting the positive regulation of excitatory postsynaptic potential were downregulated in both models. In contrast, among upregulated genes, shared GO terms and enriched pathways included categories referring to the regulation of cell differentiation, growth factor receptors, and constituents of extracellular matrix (**Figure 2B, Figure S3B, and Supplementary Table 3E-H**).

The major transcriptional changes at D28 were clustering in multiple biological processes affected in both $HNRNPU_{del/+}$ and siHNRNPU cells. We found 74 significant enriched GO terms shared between the two models, including several synaptic and transmembrane channel ontologies

among the downregulated pathways (**Supplementary Table 3I-L**). Interestingly, the shared upregulated pathways from GSEAs included pathways related to cell DNA organization during DNA replication and cell division and more general nucleosome and chromatin remodeling pathways (**Figure 2D**), confirming the role of HNRNPU in the regulation of chromatin organization and DNA replication even in neural cells. Moreover, we found that two key developmental pathways, epithelium tube and embryonic hindlimb morphogenesis, were significantly upregulated in both model systems. Additional dysregulated developmental pathways were also uniquely affected in $HNRNPU_{del/+}$ (**Figure S3C**). We also investigated whether the DEG genes at D28 were enriched in genes previously associated with epilepsies, ID, ASD, and general developmental disorders (DD). However, we found no significant enrichment for any gene lists (Hypergeometric test, **Supplementary Table 4**). These results demonstrate that *HNRNPU* deficiency modulates the transcriptomic variability by altering the expression of genes enriched in neural maturation and chromatin organization and mostly affecting cells to be committed to neuronal differentiation more than cells in the neural progenitor phase.

HNRNPU modulates exon usage of NDD genes

Since HNRNPU has previously been shown to affect the transcriptome by regulating alternative splicing (Sapir et al., 2022; Xiao et al., 2012; Ye et al., 2015), we analyzed differential exon usage (DEU), which indicates alternative splicing events or differential isoform usage. Similar to the gene level changes, we detected fewer DEU events (ExonBaseMean ≥ 10, |Log2FoldChange| > 0.58 and P adjusted < 0.05) in the earlier timepoints and more at D28 in both model systems (**Figure S3D and Supplementary Table 5**). When comparing siHNRNPU to siNTC samples, we detected 0 and 2 DEU genes at D0 and D5, respectively, whereas a comparison between $HNRNPU_{del/+}$ and CTRL yielded 35 and 38 DEU genes at D0 and D5, respectively. At D28, 976 and 1285 DEU genes were detected for siHNRNPU and $HNRNPU_{del/+}$ when compared against their respective controls, respectively. Notably, only 5.9% and 9.8% of DEU genes were also differentially expressed in siHNRNPU and $HNRNPU_{del/+}$ cells, respectively. Both models revealed more exclusion than inclusion of exons due to *HNRNPU* deficiency, as 71% of the DEU events were due to downregulation (**Figure S3D**). This result is in line with previous findings using other cell types (Huelga et al., 2012; Sapir et al., 2022; Ye et al., 2015). GSEA pathway analysis of the DEU genes shared by both models identified enriched pathways involved in cell morphogenesis,

neuron projection development, and cilium organization (**Figure 2D and Supplementary Table 6**). We also analyzed whether DEU genes were enriched for the genes implicated in the different disorders as earlier and found a strong enrichment for ID gene list (hypergeometric test followed with false discovery rate (FDR) correction: 1.49×10^{-14} and 5.26×10^{-10} for siHNRNPU and $HNRNPU_{del/+}$, respectively), ASD (8.26×10^{-8} and 1.96×10^{-7}, respectively), DD (4.68×10^{-8} and 2.36×10^{-7}), and epilepsy (2.28×10^{-6} and 0.0121) (**Figure 2E and Supplementary Table 4**). Our results demonstrate that HNRNPU is involved in regulating exon usage during neural development and that alteration of *HNRNPU* expression leads to the generation of different isoforms of genes previously associated with several NDDs.

HNRNPU deficiency increases the proportion of neural progenitor cells during differentiation

Transcriptional changes at the pathway level strongly indicated differences in the cell proliferation rate of $HNRNPU_{del/+}$ and siHNRNPU cells at D28; therefore, we focused on analyzing the neural progenitor pool at D28, a timepoint in which generally most of the cells are postmitotic and committed for neuronal maturation. First, we analyzed the cell type proportions using deconvolution of the transcriptomic data similar to what has been previously described (Becker et al., 2020). The deconvolution predicted a higher proportion of neural progenitors in $HNRNPU_{del/+}$ compared to CTRL (**Figure 3A and Figure S4A**). To validate the presence of neural progenitors across the differentiation and investigate the difference between the two models, we analyzed SOX2 positive nuclei at the three-time points for both $HNRNPU_{del/+}$ and CTRL cell lines. As expected, each cell line showed a decreased number of SOX2-positive cells during the differentiation time course. However, $HNRNPU_{del/+}$ cells displayed a significantly higher number of SOX2-positive cells at D5 and D28 compared to CTRL ($P < 10^{-4}$ and 0.002, respectively, χ^2 test) (**Figure 3B and Figure S4B**). Also, the siHNRNPU model had an increased number of SOX2-positive cells at D28, but the difference was insignificant ($P = 0.16$, χ^2 test) compared with siNTC cells (**Figure 3B**). To evaluate the rate of cell proliferation in both conditions, we measured Bromo-deoxy-uridine (BrdU) incorporation. As expected, the cell proliferation rate decreased throughout the differentiation and was significantly higher in both siHNRNPU and $HNRNPU_{del/+}$ cells at D28 compared to the relative controls at the same time point ($P = 0.002$ and 0.01, respectively, Two-sided T-test). The rate was similar between $HNRNPU_{del/+}$ and CTRL cell lines

at D0 but diverged already at D5 (P = 6x10^{-3}, Two-sided T-test) (**Figure 3C and Figure S4C**). Altogether this demonstrates that upon *HNRNPU* downregulation, the mixed population at D28 is enriched in neural progenitor cells compared with the control conditions, suggesting a delayed maturation trajectory during differentiation.

***HNRNPU* downregulation alters the maturation of neural cells**

Since the dysregulated pathways in both *HNRNPU*-deficient conditions were related to membrane channels, synaptic formation, and extracellular matrix, we hypothesized that *HNRNPU* deficiency could affect the stage of neuronal maturation. To validate this hypothesis and the transcriptomic results, we first analyzed the proportion of cells with primary cilia during neural differentiation, as primary cilia guide axon tract development (Guo et al., 2019). Additionally, our results for DEU genes showed the enrichment for cilium organization in siHNRNPU and HNRNPUdel/+ cells at D28. We, therefore, analyzed CTRL and HNRNPU$_{del/+}$ cells throughout differentiation and observed a higher number of ciliated cells at D5 compared to D0 in both cell lines and no difference between *HNRNPU* deficiency and control cells at D0 and D5 (P=0.37 and P=0.64, respectively, χ^2-test). However, a significant difference in the proportion of ciliated cells was observed at D28 (P=1.497x10-6, χ^2-test), when HNRNPU$_{del/+}$ cells had a significantly higher percentage of ciliated cells (**Figure 3D**).

Additionally, we analyzed the expression of the presynaptic marker Synapsin 1/2 and the postsynaptic marker Homer1. The HNRNPU$_{del/+}$ cells had significantly smaller presynaptic particle sizes than the CTRL cells (P = 0.009, T-test, two-sided) (**Figure 3E**). In contrast, the number of synaptic particles and the number and size of postsynaptic signals were comparable between HNRNPU$_{del/+}$ and CTRL. To monitor the neuronal maturation, we performed patch clamp electrophysiology to study the intrinsic membrane properties and synaptic activity of HNRNPU$_{del/+}$ and CTRL cells at D8 (n = 4), D28 (n = 12 cells for CTRL, and 17 cells for HNRNPU$_{del/+}$), and D50 (n = 7 cells for CTRL and 10 cells for HNRNPU$_{del/+}$) (**Figure 3F)**. However, despite the clear neuronal morphology (**Figure S4D**), the cells were characterized by high membrane resistance in response to voltage-step commands, and no spontaneous excitatory or inhibitory synaptic currents could be measured in any of the recorded cells. These results indicate that the cilia guided axonal formation and neuronal maturation process is delayed in cells with *HNRNPU* deficiency.

HNRNPU downregulation affects nuclear shape and chromatin organization

The results of our transcriptional profiling showed a role of HNRNPU in chromatin organization, in line with previous reports that demonstrated the function of HNRNPU in chromatin compaction, DNA synthesis, and chromosome folding during mitosis in different cell types and conditions (Connolly et al., 2022; Nozawa et al., 2017; Sharp et al., 2020). Therefore, we sought to investigate whether *HNRNPU* deficiency affects chromatin organization in our human neural cell model. First, we performed chromatin accessibility analyses by treating CTRL and $HNRNPU_{del/+}$ cells with DNaseI; however, no large-scale differences were visible (**Figure S5A**). We then performed single cell immunofluorescent analysis of cell nuclei stained for heterochromatin marker, histone 3 tri-methylated on lysine 9 (H3K9me3). Both *HNRNPU*-deficient cell models displayed profound changes in nuclear architecture at D28 (**Figure 4A**). Specifically, upon *HNRNPU* deficiency, a subpopulation of cells displayed differential number and total volume of heterochromatic foci (NbF, VFTotal, respectively), intensity and volume of the relative heterochromatic fraction (Intensity RHF, Volume RHF), and nuclear shape characteristics like surface area, volume, and radius of a sphere of equivalent volume (ESR) (**Figure 4A**).

Chromatin rewiring upon *HNRNPU* downregulation

Next, we performed Hi-C to investigate the changes in chromatin organization at a higher resolution (Lieberman-Aiden et al., 2009) using CTRL and $HNRNPU_{del/+}$ cells at D0 and D28 (**Figure S5B-C and Methods**). The number of chromatin interactions throughout the genome was similar at D0 between the two cell lines. However, at D28, a diverging pattern appeared in the chromatin organization maps, with the largest differences observed at the level of A/B compartments (10^5–10^6 base pairs) (**Figure S5D**). Furthermore, while the ratio of short and long-range contacts per chromosome was similar at D0, at D28 CTRL cells showed a higher ratio for the short- and long-range contacts than $HNRNPU_{del/+}$ cells (**Figure S5E**). An analysis of differential chromosome contact frequencies between the $HNRNPU_{del/+}$ and CTRL cells revealed little differences at D0 and higher contact differences at D28, as shown by the log2 ratio of the contacts at the chromosome level (**Figure 4B**).

Furthermore, a compartment interaction analysis revealed similar interaction strengths between the samples at D0 (compartmentalization strength: 1.30 and 1.28 for CTRL and $HNRNPU_{del/+}$ cells, respectively). In contrast, we observed stronger compartmentalization in

HNRNPU$_{del/+}$ at D28 (1.31 vs. 1.59 for CTRL and HNRNPU$_{del/+}$ cells, respectively), with higher interactions between active compartments (A compartment) and fewer trans-interactions compared to the CTRL cells (**Figure 4C**). These results align with the Hi-C experiments previously conducted on *Hnrnpu*-deficient mouse hepatocytes, showing decreased A-B interactions and increased A-A and B-B interactions upon *Hnrnpu* downregulation (Fan et al., 2018).

Next, we analyzed the compartment composition of each sample to identify genomic regions that switch compartments between CTRL and HNRNPU$_{del/+}$ (**Methods**). At D0, 3% of the compartments switched from inactive (B) to active (A) compartment and 5.6% from A to B comparing CTRL and HNRNPU$_{del/+}$, while at D28, 4.2% switched from B to A and 8.6% from A to B (**Figure 4D**). To investigate whether these compartment switches affect disorder-related genes, we assessed the enrichment for the genes mapping in genomic regions that switch compartments. Genes mapped in regions switching from A to B compartment were enriched in all the gene lists (ASD FDR: 0.0043; ID: 0.0018; Epilepsy: 0.0035, DD: 0.0136; hypergeometric test), whereas genes mapping in regions switching from B to A compartment were enriched only in the ASD gene list (FDR= 0.0136) (**Figure 4E and Supplementary Table 4**). In contrast, we found no GO terms significantly enriched.

Lastly, we investigated whether the compartment changes were related to the transcriptional changes described above. We, therefore, mapped the DEG at D28 (|log2FC| > 0.58, Base Mean>20) with gene mapping in the switching compartments. The concordant genes were defined as genes mapping to a region with a compartment switching from A to B and downregulated in the transcriptome analysis, or genes mapping in the B to A compartment switch and upregulated. We identified 144 concordant genes at D0 and 241 concordant genes at D28 (**Supplementary Table 7**). Only concordant genes mapping in the compartment switching from A to B at D28 were significantly enriched for ASD (FDR: 0.014) and epilepsy (FDR: 0.007) gene lists (**Figure 4E and Supplementary Table 4**). By further analyzing the concordant genes to identify the enriched pathways, we showed that no ontologies were enriched in the concordant B to A genes, while the most significant enriched GO term in the concordant A to B genes was 'GABA-gated chloride ion channel activity' (FDR < 0.05) (**Figure S5F**), driven by genes such as *CACNB2*, *GABRA2*, *GABRA4*, *GABRB1*, *GABRG1*, and *SCN1A*. Interestingly, the *GABR* family genes downregulated in HNRNPU$_{del/+}$ at D28 belong to a cluster on chromosome 4 with an

approximately seven megabase (Mb) region that maps in the A compartment in CTRL and B compartment in $HNRNPU_{del/+}$ at D28 (**Figure 4F**).

Overall, the Hi-C analysis showed that, similar to the transcriptome analyses, the compartment organization is more affected in $HNRNPU_{del/+}$ at D28 than at D0, and at both the timepoints *HNRNPU* deficiency led to an enrichment of B compartments. Interestingly, genes mapping in the enriched B compartments are associated with ASD and epilepsy, suggesting that the chromatin remodeling dependent on HNRNPU expression might ultimately be the driver of the observed phenotypes.

DISCUSSION

Heterozygous genetic variants in the *HNRNPU* gene lead to various disorders with predominant brain phenotypes. However, the exact role of this gene in human neural development has not been studied before. Here, we provide novel evidence of the molecular and cellular consequences of *HNRNPU* deficiency in human neuronal cells, demonstrating that adequate levels of *HNRNPU* are needed in the early developmental transition from neural progenitors to developing neurons for proper neurogenesis. Our results, consistent with the earlier reports, show that *HNRNPU* expression is highest at early neural stem cell and progenitor stages and in a subpopulation of neural progenitors at the later stage of neuronal differentiation (Connolly et al., 2022; Sapir et al., 2022). Despite this high expression, results indicate that *HNRNPU* deficiency does not affect neural cells at this early stage.

In contrast, as the neural progenitor cells commit to differentiation, the reduced *HNRNPU* levels led to a higher number of dividing neural progenitors compared to the control stage, in a phase where the proportion of progenitor cells should decrease. This delayed transition from progenitors to differentiating neurons could explain the lack of differences in *HNRNPU* expression in $HNRNPU_{del/+}$ from D0 and D5, and the almost equal expression levels with CTRL cells at D28, despite the heterozygous deletion of one allele. A recent study showed opposite effects for the complete loss of *Hnrnpu*, as it led to decreased proliferation followed by cell death of neural progenitors and postmitotic neurons in mice (Sapir et al., 2022). As heterozygous mutations in *HNRNPU* are not lethal, and the severity of the phenotypes in *HNRNPU*-related disorders is variable (Balasubramanian, 2022), embryonic cells can likely adapt to low levels of *HNRNPU* and still proliferate and differentiate. Therefore, it is reasonable that iPSCs and NES cells that retain

30–70% of the physiologic *HNRNPU* levels do not show a major phenotype, as we have shown here. Instead, we propose that cells with *HNRNPU* haploinsufficiency are inadequate to drive efficient cell fate transition of mitotic cells into maturing neurons and other neural cells through multiple regulatory pathways, leading to stochastic rewiring of brain development. Indeed, altered regulation of proliferation has been demonstrated to cause defects in the progenitors' fate and, ultimately, neuronal development trajectories (Pilaz et al., 2016). In several cellular models of ASD, both hyper- and hypo-proliferation of neural progenitors have been documented (Connacher et al., 2022; Marchetto et al., 2017; Mowat et al., 2003; Zucco et al., 2018).

We provide mechanistic insights into that both RNA processing and chromatin regulation in early brain development play a critical role in the observed brain phenotypes in *HNRNPU*-related disorders. It has been earlier demonstrated that the correct pool of mRNA isoforms from the alternative splicing process is important in the transition from progenitor cells to neurons in the developing cerebral cortex (Zhang et al., 2016), and RNA splicing is one of the key enriched pathways from molecular and genetic studies of ASD (Gandal et al., 2018; Satterstrom et al., 2020). Therefore, our and others' results pinpoint that further delineation of the RNA splicing program during the early steps of brain development is essential for understanding the origins of NDDs.

Furthermore, the importance of 3D genome organization for cell fate decisions during neural development is starting to emerge, showing that dynamic changes at multiple levels of chromatin organization are needed for these processes (Bonev et al., 2017; Hu et al., 2021). This is in line with our results showing major reorganizations related at a later stage of neural differentiation. Indeed, multiple NDD cell models have shown that the dysfunction of the chromatin organization leads to changed neuronal maturation (Calzari et al., 2020; Parisian et al., 2020; Su et al., 2021).

We additionally provide evidence of cellular processes, such as cilia organization and synaptogenesis, that are affected by the molecular changes in the *HNRNPU*-deficiency state. For instance, we demonstrate an increase in ciliated cells. Recently, HNRNPU was indicated to localize occasionally to cilium in mice brain cells (Sapir et al., 2022). As *HNRNPU*-related disorders share many phenotypic features with ciliopathies (Balasubramanian, 2022; Focșa et al., 2021), the connection between cilia organization and *HNRNPU* warrants more studies.

In conclusion, we provide the first evidence of the functional consequences of *HNRNPU* mutations in human neural progenitors in the form of an inadequate switch to neurogenesis. This, in turn, leads to large-scale effects on chromatin organization and transcriptional landscape at later stages of neural development and presumably to diverging trajectories of neurons and other neural cells. Follow-up studies based on organoid models rather than 2D cell cultures will be needed to assess better the impact of *HNRNPU* haploinsufficiency on neurogenesis and its role in the pathogenesis of *HNRNPU*-related disorders.

LIMITATIONS OF THE STUDY

We acknowledge that this study has limitations, including that we only compare the isogenic model constructed with siRNA with one patient cell line, providing the limited possibility to analyze the genomic background effects, recently shown to be highly important to study (Paulsen et al., 2020). Furthermore, we focused on a very early model of neural development using NES cells and undirected differentiation, which cannot represent the complexity of the human brain. Further studies on human organoids should be employed to present the effects of HNRNPU mutations in later stages of brain development.

AUTHOR CONTRIBUTIONS

Conceptualization: F.M., M.O., and K.T.; Methodology and Data Analysis: F.M., M.O., C.S., S.A., A.A., R.B., M.M., F.A., A.P., M.W., I.R., M.B., D.L., B-M.A., J.I., K.L.R., Mo.M., Y.J., A.F., A.B., and K.T.; Validation: F.M., M.O., C.S., S.A., A.A., and K.T.; Resources: S.B. and K.T.; Data Curation: F.M., M.O., A.A., F.A., A.P., M.W., D.L., B.M.A., J.I., K.L.R.; Writing – Original Draft: F.M. and K.T.; Writing – Review & Editing: F.M., M.O., and K.T.; Visualization: F.M., M.O., D.L., and K.T.; Supervision: Y.J., N.C., M.Bi., E.S., A.B., and K.T.; Project Administration: F.M. and K.T.; Funding Acquisition: F.M., Y.J., N.C., E.S., A.B., S.B., and K.T., Critical review of the draft: All authors.

ACKNOWLEDGMENTS

The authors are grateful to the donors of the cell lines for their participation in this research. The authors acknowledge support from the National Genomics Infrastructure in Stockholm funded by Science for Life Laboratory, the Knut and Alice Wallenberg Foundation and the Swedish Research

Council, the SNIC/Uppsala Multidisciplinary Center for Advanced Computational Science for assistance with massively parallel sequencing and access to the UPPMAX computational infrastructure, A. Smialowska and NBIS (National Bioinformatics Infrastructure Sweden) for technical support with HiC data analysis and the iPS Core facility at Karolinska Institutet for assistance with the generation of iPSC and NES cells. The project was supported by grants from the Swedish Research Council to K.T. (grant no. 2017-01660), S.B. (grant no. 2019-01303), and N.C. (grant no. 2018-02950); the., A.F.), Swedish Foundation for Strategic Research to K.T. (grant no. FFL18-0104); the Swedish Brain Foundation – Hjärnfonden to K.T.; the Karolinska Institutet KID Program to N.C., KI-NIH PhD program for PhD students (M.O.), Osk. Huttunen Foundation (M.O.), Åke Wiberg Foundation to K.T.; the H.K.H. Kronprinsessan Lovisas förening för barnasjukvård och Stiftelsen Axel Tielmans minnesfond to F.M.; the Swedish Foundation for Medical Research (SSMF) to F.A.; The Foundations of Petrus och Augusta Hedlund to K.T.; the Strategic Research Area Neuroscience (StratNeuro) at Karolinska Institutet to K.T.; the Swedish Foundation for International Cooperation in Research and Higher Education (STINT) to K.T.; and the Committee for Research at Karolinska Institutet to K.T., grant #R35GM128661 from the National Institutes of Health (Y.J.). Open access funding is provided by Karolinska Institutet.

DECLARATION OF INTERESTS

M.B. is a full-time employee of Bayer AG, Germany. S.B. declares no direct conflict of interest related to this article. He discloses that he has, in the last 3 years acted as an author, consultant, or lecturer for Medice and Roche. He receives royalties for textbooks and diagnostic tools from Hogrefe, and Liber. S.B. is shareholder in SB Education/Psychological Consulting AB and NeuroSupportSolutions International AB. The other authors have no conflicts to declare.

FIGURE LEGENDS

Main figures

Figure 1. *HNRNPU* expression changes during neural differentiation and brain development. A) Schematic summary of the samples and methods used in the study. **B)** *HNRNPU* RNA expression in CTRL and $HNRNPU_{del/+}$ at D0, D5, D28. The full lines indicate the comparisons between the time points for each cell line; the black dotted line indicates the comparison between the two cell lines at each time point. **C)** *HNRNPU* RNA expression in all the

brain regions during development from Human Brain Transcriptome dataset. The vertical line indicates the time of birth. AMY= Amygdala, CBC= Cerebellar Cortex, HIP= Hippocampus, MD= Mediodorsal nucleus thalamus, STR= Striatum **D)** *HNRNPU* RNA expression in neurotypical samples from published iPSC- neuronal study dataset (Burke et al., 2020). The day 0 refers to rosette forming cells comparable to NES cells and the following time points are days of differentiation. *$p<0.05$; ***$p<1x10^{-4}$; ****$p<1x10^{-5}$. In the figure, the $HNRNPU_{del/+}$ samples are indicated as "HNRNPUdel".

Figure 2. *HNRNPU* expression affects cell differentiation pathways and modulates exon usage of NDD genes. A-B) Top 10 upregulated and downregulated GO terms from ranked differentially expressed genes in siHNRNPU (left panel) and $HNRNPU_{del/+}$ (right panel) at D0 (A) and D5 (B). **C)** Selected upregulated (left panel) and downregulated (right panel) pathways enriched at D28. For each node, the left half indicates the enrichment in siHNRNPU versus siNTC, and the right half the enrichment in $HNRNPU_{del/+}$ versus CTRL. The color of the edge indicates which of the datasets significantly contributed to the pathway call (p adj <0.05). **D)** Top 20 GO terms enriched from genes with differential exon usage in siHNRNPU (left panel) and $HNRNPU_{del/+}$ (right panel) at D28. **E)** Enrichment of genes subject to differential exon usage (DEU) in siHNRNPU versus siNTC (cyan) or $HNRNPU_{del/+}$ versus CTRL (magenta) in ASD, ID, epilepsy (EPI), DD gene lists at D28. The vertical dotted line represents the significance threshold of FDR<0.05 (-log10(FDR)>1.3) after hypergeometric analysis. In the figure, the $HNRNPU_{del/+}$ samples are indicated as "HNRNPUdel".

Figure 3. Cells at the late-differentiation stage show higher progenitor phenotype and affected synaptogenesis under *HNRNPU* downregulation. A) Neural progenitor cells proportion in siNTC, siHNRNPU, CTRL, $HNRNPU_{del/+}$ at D28 estimated by deconvolution analysis. **B)** Percentage of cells positive at the staining with SOX2 antibody at D28. **C)** Proliferation rate of siNTC, siHNRNPU, CTRL, $HNRNPU_{del/+}$ at D28. **D)** Immunofluorescence of primary cilia with ciliary marker ARL13B and basal body marker PCNT in CTRL and $HNRNPU_{del/+}$ and quantification of ciliated cell proportions. Pictures were acquired with 63X magnification, 0.5 zoom and z-stack. Scale bar= 20 µm. **E)** Immunofluorescence of synapsin1/2 in CTRL and $HNRNPU_{del/+}$ at D28 and quantification of the mean size of the synapse particles

positive to synapsin1/2 staining. Pictures were acquired with 63X magnification and z-stack. Scale bar= 20 µm. **F)** Electric properties of the membrane of CTRL and $HNRNPU_{del/+}$ cells at different time points. *$p < 0.05$, **$p < 0.001$, *** < 0.0001. In the figure $HNRNPU_{del/+}$ samples are indicated as "HNRNPUdel".

Figure 4. *HNRNPU* downregulation affects chromatin organization. A) Biplot of the contribution of the variables generated by NucleusJ for the clustering of the nuclei after H3K9me3 staining, compared siHNRNPU with siNTC (left panel) and $HNRNPU_{del/+}$ with CTRL (right panel). **B)** Example of normalized log2ratio of the contacts for each chromosome of $HNRNPU_{del/+}$ compared with CTRL, at D0 and D28, after ICE correction. **C)** Saddle plot of the *cis*- and *trans*-interactions of the A (active) and B (inactive) compartments in CTRL and $HNRNPU_{del/+}$ at D28. **D)** Genome-wise compartment switch at D0 and D28 in the comparison for each time point of $HNRNPU_{del/+}$ and CTRL. **E)** An enrichment of genes within the compartment switch regions in ASD, ID, epilepsy (EPI), and DD gene lists at D28. "Expressed", indicated by the dotted pattern, include genes that map in one of the compartment switches and are expressed in our dataset (Gene count > 20 in at least one sample). "Concordant", indicated by the vertical lines pattern, includes the genes that are upregulated from the transcriptome analysis and map in a compartment B in CTRL and A in $HNRNPU_{del/+}$ or vice versa. The vertical dotted black line represents the significance threshold of FDR<0.05 (-log10(FDR)>1.3) after the hypergeometric test corrected for all the comparisons. **F)** Representative compartment switch from A to B at D28 between CTRL and $HNRNPU_{del/+}$ on chromosome 4. The upper panel shows the eigenvectors of the first 90 Mb of chr 4 for each sample (yellow for $HNRNPU_{del/+}$ and blue for CTRL). The zoom-in panel shows the eigenvectors of the two samples in the chromosome location of chr4: 43-49 Mb. The lowest panel shows the genes mapping onto the switch region (Dark blue: downregulated genes in the $HNRNPU_{del/+}$ -CTRL comparison; light blue: expressed in the dataset but not differentially expressed in the two conditions; light green: not expressed). In the figure $HNRNPU_{del/+}$ samples are indicated as "HNRNPUdel".

Supplementary Figures

Figure S1. Characterization of the two *HNRNPU* knockdown conditions. A) HNRNPU protein expression after treatment with siHNRNPU at D0. Bar plot normalized for each siNTC

sample. **B)** HNRNPU protein expression after treatment with siHNRNPU at D28. Bar plot (left) normalized for each siNTC sample. Capillary western blot representation (right) of the samples probed with antibody against HNRNPU and total protein quantification in the following lanes. **C)** Karyotype of iPSCs obtained from the fibroblasts of the individual carrying the heterozygous deletion of HNRNPU, and from which the $HNRNPU_{del/+}$ cells were derived. **D)** Staining the $HNRNPU_{del/+}$ -iPSC cells with the pluripotency markers OCT4 and NANOG. Nuclei are counterstained with DAPI. **E)** Immunostaining of SOX2 and NESTIN in $HNRNPU_{del/+}$ cells at D0. Scale bar= 50µm. **F)** Quantification of HNRNPU protein at D0 in CTRL and $HNRNPU_{del/+}$. Capillary western blot representation of the samples probed with antibody against HNRNPU and total protein quantification in the following lanes. Quantification graph on the right panel. **G)** UMAP dimensional reduction of single-cell RNAseq data from previously published cells at D28, obtained with the same differentiation protocol as the cell model in study (Becker et al., 2020). The different cell type clusters are highlighted. **H)** Feature plot of HNRNPU expression in the cell clusters from the single-cell RNAseq analysis **I)** Violin plot of HNRNPU expression in each cell cluster from the single-cell RNAseq analysis. **J)** Expression of proliferation markers in the subclusters defining the NPCs subpopulation from the single-cell RNAseq analysis. 0-1-2 refer to the NPCs subpopulations showed in H. In the figure $HNRNPU_{del/+}$ samples are indicated as "HNRNPUdel".

Figure S2. HNRNPU protein localization and expression during neuronal differentiation. A) Immunostaining of HNRNPU in red, Hoechst in blue and merge at D0, D5 and D28 in CTRL and $HNRNPU_{del/+}$. Scale bar= 10 µm. **B)** HNRNPU protein quantification during differentiation in CTRL and $HNRNPU_{del/+}$. In the figure $HNRNPU_{del/+}$ samples are indicated as "HNRNPUdel".

Figure S3. Extended differential pathway enrichment under HNRNPU downregulation during neurodevelopment. A-B) All the upregulated and downregulated pathways, respectively, at D0 and D5. **C)** Upregulated pathways at D28 related to general development. For each node, the left half indicates the siHNRNPU versus siNTC enrichment and the right half the $HNRNPU_{del/+}$ versus CTRL enrichment. The color of the edge indicates which of the datasets significantly contributed to the pathway call. **D)** Volcano plots of DEU exon bins at D0, D5 and D28 for both HNRNPU deficient conditions. The plots are zoomed in, and some highly significant exon bins

are thus excluded from the D28 plots to enhance readability. In red is the upregulated DEU, and in blue is the downregulated DEU. The vertical lines indicate the threshold for significance (p adj < 0.05 and |log2FoldChange|>0.58). In the figure $HNRNPU_{del/+}$ samples are indicated as "HNRNPUdel".

Figure S4. Delayed maturation and higher progenitor phenotype under HNRNPU downregulation during the differentiation time course

A) Estimated proportion of the different cell types at D28 after deconvolution analysis. **B)** SOX2 positive cells at D0 and D5 in CTRL and $HNRNPU_{del/+}$. **C)** BrdU signal at D0 and D5 in CTRL and $HNRNPU_{del/+}$. **D)** MAP2, HNRNPU and Hoechst staining of CTRL and $HNRNPU_{del/+}$ at D28. Scale bar= 50µm. *p<0.05. In the figure $HNRNPU_{del/+}$ samples are indicated as "HNRNPUdel".

Figure S5. Extended effects of HNRNPU downregulation on chromatin organization. A) DNaseI sensitivity assay in CTRL and $HNRNPU_{del/+}$. **B)** Heatmap of the correlation matrixes of the HiC samples. **C)** Pearson's correlation matrixes of the HiC samples. **D)** Corrected HiC counts at a specific genomic distance at D0 (left) and D28 (right). **E)** Boxplot of short range/long range HiC contact per chromosome. **F)** Pathways enriched in the "concordant A to B" genes, according to Over-representation analysis from WebGestalt. In the figure $HNRNPU_{del/+}$ samples are indicated as "HNRNPUdel".

KEY RESOURCES TABLE

REAGENT or RESOURCE	**SOURCE**	**IDENTIFIER**
Chemicals, Peptides, and Recombinant Proteins		
DMEM/F-12 Glutamax	Thermo Scientific	31331-093
Penicillin/ Streptomycin	Thermo Scientific	15140122
Laminin from Engelbrecht-holm-swarm murine cells	Sigma-Aldrich	L2020
B-27 Supplement	Thermo Scientific	17504044
N-2 Supplement	Thermo Scientific	17502001

Poly-L-ornithine	Sigma Aldrich	P3655
Bovine serum albumin	Sigma Aldrich	A7030
DNase I	Thermo Scientific	EN0521
Accell SMARTpool si-HNRNPU	Dharmacon	E-013501-00-0010
Accell SMARTpool si-NTC	Dharmacon	D-001950-01-20
Neural isolation enzyme	Thermo Scientific	88285
TrypLE express	Gibco	12604013
Diamond Antifade Mountant	Thermo Scientific	15205739
Anti-H3K9me3 Antibody	Abcam	Ab6000
Anti-Nestin Antibody	Merck-Millipore	MAB5326-KC
Anti-SOX2 Antibody	Merck-Millipore	AB5603
Anti-HNRNPU Antibody	Novus Biologicals	NBP2-49290
Anti-MAP2 Antibody	Merck-Millipore	M2320
Anti-SYNAPSIN1/2 Antibody	Synaptic System	106006
Anti-HOMER1 Antibody	Synaptic System	160011
Anti-ARL13B Antibody	Proteintech	17711-1-AP
Anti-PCNT Antibody	Abcam	Ab28144
Anti-mouse AlexaFluor488	Invitrogen	A21202
Anti-rabbit AlexaFluor555	Invitrogen	A31572
Anti-chicken AlexaFluor488	Jackson Immuno research	703-545-155
Anti-mouse CF555	Biotium	20037
Critical Commercial Assays		
Arima-HiC kit	Arima Genomics	A510008

BrdU Assay	Abcam	ab126556
ReliaPrep RNA Miniprep	Promega	Z6012
Total Protein Detection Module for Jess, Wes, Peggy Sue, or Sally Sue	Biotechne	DM-TP01
EZ Standard pack WES	Biotechne	PS-ST01EZ-8
Deposited Data		
RNAseq and HiC analysis pipeline	GitHub	https://github.com/Tammimies-Lab/HNRNPUdeficiency-Mastropasqua-et-al.
Software and Algorithms		
R (v4.1.2)	R	r-project.org
DESeq2 (v1.34)	Bioconductor	10.18129/B9.bioc.DESeq2
Cytoscape (v3.9.0)	Cytoscape	cytoscape.org
EnrichmentMap (v3.3.3)	Cytoscape	10.1371/journal.pone.0013984
GSEA (v4.2.1)	Broad Institutet	10.1073/pnas.0506580102
AutoAnnotate (v1.3.5)	Cytoscape	10.12688/f1000research.9090.1
ggplot2 (v3.3.5)	CRAN	ggplot2.tidyverse.org
DEXSeq (v1.40)	Bioconductor	10.18129/B9.bioc.DEXSeq
HiCExplorer (v 3.7)	HiCExplorer	10.1038/s41467-017-02525-w
FanC (v 0.9.2)	FanC	10.1186/s13059-020-02215-9
WebGestaltR (v0.4.4)	CRAN	https://doi.org/10.1093/nar/gkz401

LEAD CONTACT AND MATERIALS AVAILABILITY

Further information and requests for resources and reagents should be directed to and fulfilled by the Lead Contact, Kristiina Tammimies (kristiina.tammimies@ki.se).

DATA AND CODE AVAILABILITY

All the related code and data matrixes are available in the GitHub https://github.com/Tammimies-Lab/HNRNPUdeficiency-Mastropasqua-et-al.

METHODS

Identification of the individuals with *HNRNPU* deletion and phenotypic characterization

We have earlier performed a screening for copy number variation in a twin sample from The Roots of Autism and ADHD study in Sweden (RATSS) (Bölte et al., 2014; Stamouli et al., 2018) in which we identified a male twin pair carrying the deletion on chr1:244997953-245042312 (hg19) encompassing *HNRNPU*. The twin pair has undergone an extensive phenotypic characterization, including evaluation for ASD, ID, and other NDDs, cognitive testing, and medical examination (Supplementary table 1). Written informed consent was obtained from individuals and their parents prior to the study. The study was approved by the regional and national ethical boards in Sweden and has been conducted in accordance with the Declaration of Helsinki for medical research involving human subjects, including research on identifiable human material and data.

Cell culture

Human iPSC cells were derived from fibroblasts of a male carrying a 44Kb mutation of the HNRNPU locus spanning through *COX20*, *AS1-HNRNPU,* and *HNRNPU*, using a previously described protocol (Uhlin et al., 2017b). Pluripotency and normal karyotype were confirmed, as shown in Supplementary Fig 1. Dual-SMAD inhibition was applied to derive neuroepithelial stem (NES) cells from human iPS cells as described previously (Chambers et al., 2009; Falk et al., 2012). Patient-derived and previously established NES cells from a male neurotypical donor (Uhlin et al., 2017a) were seeded on 20 µg/ml poly-L-ornithine (Sigma Aldrich), and 1 µg/ml laminin (Sigma Aldrich) precoated plastic surfaces in DMEM/F12 + Glutamax medium (Gibco) supplemented with 0.05X B-27 (Gibco), 1X N-2 (Gibco), 10 ng/ml bFGF (Life Technologies), 10 ng/ml EGF (PeproTech) and 10 U/ml penicillin/streptomycin (Gibco), replacing media every day. For immunofluorescence, the glass coverslips were precoated with increased concentrations of poly-L-ornithine to 100 µg/ml and laminin to 2 µg/ml. Cells were maintained in a 5% CO_2 atmosphere at 37°C. Upon starting the differentiation, cells were changed to medium with an increased 0.5X B-27 concentration without bFGF and EGF. Two-thirds of media supplemented with 0.4 ug/ml laminin was changed every other day until differentiation 15; whereafter media was changed every third day. NES cells were harvested two days after culturing and neural cells were harvested after 5, 28 or 50 days of differentiation.

DNAse I sensitivity assay

Cells were grown and harvested as earlier described and resuspended in cold RSB buffer: 10mM Tris-HCl (pH7,4), 10mM NaCl, and 3mM $MgCl_2$. Cells were then lysed in cold lysis buffer (RSB buffer and 0,2% Triton X-100) and centrifuged to collect nuclei in the pellet. The nuclei were then incubated with different amounts of DNase I enzyme (0, 1, 3, 5, 0, 15 units) at 37°C for 10 min. The digestion was blocked by adding 50mM of EDTA followed by incubation at 55◦C for 1min. The results of the digestion were visualized on an 0.8% agarose gel.

siRNA-mediated silencing

Cells were transfected with 0.5 µM Accell SMARTpool siRNA targeting *HNRNPU* mRNA (Dharmacon E-013501-00-0010) or 0.5 µM Accell Nontargeting siRNA (Dharmacon D-001950-01-20) according to manufacturer's protocol. The siRNA pool consisted of the following oligos: oligo1: UCUUGAUACUUAUAAUUGU, oligo2: CUCGUAUGCUAAGAAUGGA, oligo3: GUUUCAGGUUUUGAUGCUA, oligo4: CUAGUGUGCUUGUAGUAGU. NES cells were transfected one day after seeding, and samples were collected 24 hours after treatment. Cells under differentiation were transfected once in the NES phase, once when changing media to differentiation media, and thereafter every sixth day until D28 sample harvesting.

Immunofluorescence and image analysis

Cells on glass coverslips were fixed in 4% formaldehyde for 20 minutes at room temperature and washed with 1X TBS. Blocking was performed with 5% Donkey Serum and 0.1% Triton X-100 in 1X TBS for 1 hour. Primary antibodies diluted in blocking buffer (Nestin 1:1000; SOX2 1:1000; Synapsin ½ 1:500; Homer1 1:250; MAP2 1:500; HNRNPU 1:500; H3K9me3 1:500, ARL13B 1:10000, PCNT 1:250) were incubated at +4ºC overnight. Careful washing was done with 1X TBS, and secondary antibodies diluted 1:1000 in blocking buffer were incubated at room temperature for one hour, covered from light. Coverslips were washed and mounted with Diamond Antifade Mountant (Thermo Scientific). Images were acquired with LSM 700 Zeiss Confocal Microscope using 20x or 63x magnification and 0.5 µm z-stack through the sample.

At least three replicates per sample were stained and analyzed for the immunocytochemistry analyses. The images stained with synapsin 1/2 were analyzed with ImageJ plugin Synapse Counter, and the statistical Student T-test analyses were performed in R. The

statistical analyses for SOX2 positive nuclei were performed in R by χ^2-test. For primary cilia analysis, a cell was considered ciliated if positive for both cilia markers ARL13B and PCNT; the statistical testing was performed in R by χ^2-test. For the images of the nuclei stained with the H3K9me3 antibody, the single nuclei were cropped using an in-house built macro for ImageJ. A minimum of thirty nuclei per replicate was analyzed with NucleusJ, a plugin of ImageJ, using the default settings (Poulet et al., 2015).

Capillary Western blot

Cells were collected in extraction buffer (50 mM Tris-HCl, 100 mM NaCl, 5 mM EDTA, 1 mM EGTA) supplemented with a 1X protease inhibitor cocktail (Thermo Scientific) using a plastic cell scraper. The samples were sonicated with six short pulses at 36% amplitude (Vibra-Cell VCX-600, Sonics). Protein concentrations were measured with Qubit Protein Assay Kit (Thermo Scientific). The total protein sample (150 ng/µl) was loaded on the capillary western blot system Simple-Western-JESS (Bio Techne), multiplexed for total protein and chemiluminescence detection of HNRNPU (1:10 dilution). Data were analyzed using Compass for S.W. software (5.0.1), and the HNRNPU peak area was normalized against the total protein area. Three to five biological replicates were analyzed for each time point, and the significance at each time point was evaluated by Student T-test.

RNA extraction and bulk RNA sequencing analyses

Cells were lysed in TRIzol reagent (Invitrogen), and RNA isolated with ReliaPrep RNA Cell Miniprep kit (Promega Z6012). We extracted RNA samples for three to five biological replicates per cell line and time point. Samples were delivered to NGI Sweden for library preparation and sequencing. The samples were subjected to library preparation with Illumina Truseq Stranded total RNA RiboZero GOLD kit, except for siNTC-D28 and siHNRNPU-D28 libraries prepared with Illumina TruSeq Stranded mRNA kit due to low RNA yields. All libraries were sequenced on the NovaSeq6000 platform with a 2x151 setup using NovaSeqXp workflow in S4 mode flowcell. We obtained, on average, 35 and 65 million reads per sample for early time points and D28, respectively, with a minimum 82,7% alignment rate.

Differential gene expression analysis was performed using DESeq2 (v1.24.0) (Love et al., 2014) in R (v4.1.2). The significance thresholds used were adjusted p value < 0.05 (Benjamini-

Hochberg adjustment), base mean > 20, and absolute log2 fold change > 0.58. Pathway analysis was done according to previously described protocols (Reimand et al., 2019). In short, the ranked gene expression list was used in Gene set enrichment analysis (GSEA) (Version 4.3.0) to analyze the enrichment in the gene ontology, molecular function, and biological process gene lists (v. 7.4), and enriched categories were visualized in Cytoscape (v3.8.2) with Enrichment Map (v3.1.0) and AutoAnnotate (Merico et al., 2010; Shannon et al., 2003).

Differential exon usage analysis was performed using the DEXSeq package (v1.40.0) (Anders et al., 2012). A flattened annotation file was created using provided python script, excluding the aggregate exon bins, and exon counts were counted using provided python script. The analysis was performed with the formula *~ sample + exon + condition: exon.* A gene was called to have evidence for DEU if at least one exon bin was differentially used between conditions. The difference was considered significant with FDR (Benjamini-Hochberg adjustment) adjusted P<0.05, exon base mean >10, and an absolute log2 fold change>0.58. Over-representation analysis (ORA) was performed using the online tool WebGestalt (Liao et al., 2019). In addition, hypergeometric tests were used to test for enrichment between differentially expressed genes and DEU genes and specific NDD-related gene lists: ASD gene list (SFARI genes selected for score 1,2 and syndromic, release 07-20-2022), ID gene list (green and amber genes from https://panelapp.genomicsengland.co.uk/ v3.1632), epilepsy gene list (green and amber genes from https://panelapp.genomicsengland.co.uk/ v2.547) and general development (compiled gene list (Becker et al., 2020)).

Hi-C sequencing

Cells were cultured as NES for D0 collection or differentiated for 28 days and harvested by briefly rinsing the cells in accutase and then incubating them with TrypLE express (Gibco) and neural isolation enzyme (Thermo Scientific). Samples were then processed using the Arima-HiC kit (PMID: 29779944) according to the Arima Genomics User Guide for Mammalian Cell Lines (Catalog number A510008). Briefly, we crosslinked harvested cells with 2% formaldehyde and then used approximately 1 million fixed cells as input for each replicate sample. Subsequently, we used 1.5 µg of Hi-C template for biotin pull-down and library preparation according to the Arima Genomics User Guide for Library Preparation using KAPA Hyper Prep Kit. Specifically, we used 8 PCR cycles for library amplification. We then sequenced the Arima-HiC libraries for each time

point on one flowcell on the Illumina NovaSeq S Prime system, obtaining an average of 900M sequencing reads for D0 samples, and 1000M sequencing reads per sample for D28 samples. Sequencing was carried out at the National Genomics Infrastructure at the Science for Life Laboratory (SciLifeLab) in Stockholm, Sweden.

We processed the raw sequencing reads using the HiCUP pipeline (v0.7.4) (PMID: 26835000) with default parameters. Briefly, the pipeline employs Bowtie2 (v2.4.1) (PMID: 22388286) to align the reads to the human reference genome (GRCh37/hg19) and filter out experimental artifacts (i.e., circularised, re-ligated, and duplicate reads). We generated the 'digest file' using the 'hicup_digester' command with the Arima option (--Arima). We used the HiCUP output files (BAM format), which contain only valid, non-redundant read pairs, as input for pairtools (v0.3.0). First, we converted the BAM files into .pairsam format using the pairtools parse and sort modules. In addition to individual replicates, we generated pooled samples for each developmental stage by merging replicates using the pairtools merge module. We marked read duplicates using the pairtools dedup module, with option --mark-dups, and filtered the results by selecting only specific pair types (i.e., 'U.U.', 'U.R.' and 'R.U.') via the pairtools select module, which produced a .pairs format output. Finally, we added the fragment information using the 'fragment_4dnpairs.pl' convenience script provided alongside the Juicer pipeline and converted the .pairs files into .hic format using the Pre module from Juicer-Tools (v1.22.01). Unless explicitly required by the software/package, the contact matrices were normalized to the smallest library and corrected with ICE using HiCexplorer (v 3.7) (Ramírez et al., 2017). HiCexplorer package was used for mapping genomic contacts and contact enrichment between the samples.

The compartments were called at 1 Mb resolution, and the first four PCAs were extracted by HiCexplorer using the hicPCA tool and the gene track from hg19 to assure the correct orientation of the eigenvector. The PCA for each chromosome and each sample were chosen by considering the highest correlating PCA between the samples and the best mapping with the gene density eigenvector. The compartments were defined as A and B according to the eigenvector orientation, with A being the gene-rich and positive eigenvector and B being the gene-poor regions and negative eigenvector. FanC toolkit (v. 0.9.1) (Kruse et al., 2020) was used to calculate compartment strength and cis-trans- compartment interactions. The R package annotatr was used to annotate the genomic regions switching compartments in the different conditions.

Deconvolution

The deconvolution of bulk RNASeq data to previously published single-cell RNA sequencing sample (Becker et al., 2020) was done using the Bseq-SC package (Baron et al., 2016). Bseq-SC uses cell-type-specific marker genes from single-cell RNA transcriptomes to predict cell-type proportions underlying bulk RNA transcriptomes. Deconvolution was done with 30 marker genes for each cell population, except for cluster "Undefined maturing neurons", which had only 25 defining genes. Statistical differences in the estimated cell proportions were calculated by the χ^2 statistical test in R (v4.1.2).

Public data processing

Data from Human Brain Transcriptome (https://hbatlas.org) were obtained to visualize *HNRNPU* expression in different human brain regions during development. Additional stem cell time-course data was accessed via LIBD Stem Cell Browser (http://stemcell.libd.org/scb). RPKM values for HNRNPU were extracted for evaluating *HNRNPU* expression during neuronal differentiation from iPSCs (Burke et al., 2020).

Cell proliferation assay

To analyze differences in cellular proliferation, the BrdU assay (ab126556, Abcam) was performed for three replicates at D0, D5, and D28 time points. Twenty-four hours prior to the read-out, 1X-BrdU reagent was added to the cell culture vessels for incorporation by incubation at 37°C and 5% CO_2. The culture media was aspirated for the read-out, and cells were fixed with the supplied fixing solution. This was followed by exposure to the anti-BrdU antibody (primary antibody), incubation at room temperature for 1 hour, and washing with the supplied plate wash buffer. The cells were incubated with the HRP-tagged secondary antibody at room temperature for 30 minutes, followed by TMB exposure and recording absorbance at 450 nm. Afterwards, the cells were incubated in TBS, 0.1% triton-X 100, and Hoechst 1:1000 for 15 min, followed by fluorescence measurement, which was used to calibrate the BrdU quantification for the number of nuclei in each sample. The quantification of proliferation rate followed by Student T-test statistical comparison was done in R (v4.1.2).

Electrophysiology

Whole-cell patch-clamp recordings were performed at 5, 8, 28, and 50 days of differentiation. Immediately prior to recordings, the cells were washed with 1X PBS, and then Krebs-Ringer's solution composed of (in mM): NaCl 119, KCl 2.5, NaH2PO4 1, CaCl2·2H2O 2.5, MgCl2·6H2O 1.3, HEPES 20, D-Glucose 11 (pH 7.4) + Laminin 1:1000 was added in the dish. The recordings were performed in Krebs-Ringer's solution. Recording pipettes were fabricated with a Narishige pc-100 puller and had resistances of 3-5 MOhm when filled with the internal solution composed of (in mM): 120 K-gluconate, 0.1 EGTA, 4 MgATP, 0.3 Na2GTP, 10 HEPES, 20 KCl and 5 Na2-phosphocreatine (pH 7.4). Current and voltage responses were measured at room temperature using a MultiClamp 700B amplifier (Molecular Devices) and digitized with Axon™ Digidata® 1550B analog-to-digital converter connected to a personal computer running pClamp 11.0.3 (Molecular Devices). Membrane capacitance and resistance were derived from the pClamp 11.0.3 (Molecular Devices) membrane-test function. Data analysis was performed by Clampfit 10.7 (Molecular Devices).

SUPPLEMENTAL INFORMATION

Supplemental information can be found online at BioRxiv.

References

Anders, S., Reyes, A., and Huber, W. (2012). Detecting differential usage of exons from RNA-seq data. Genome Res *22*, 2008–2017. https://doi.org/10.1101/gr.133744.111.

Balasubramanian, M. (2022). HNRNPU-Related Neurodevelopmental Disorder. In GeneReviews®, M.P. Adam, D.B. Everman, G.M. Mirzaa, R.A. Pagon, S.E. Wallace, L.J. Bean, K.W. Gripp, and A. Amemiya, eds. (Seattle (WA): University of Washington, Seattle), PMID: 35274911

Baron, M., Veres, A., Wolock, S.L., Faust, A.L., Gaujoux, R., Vetere, A., Ryu, J.H., Wagner, B.K., Shen-Orr, S.S., Klein, A.M., et al. (2016). A Single-Cell Transcriptomic Map of the Human and Mouse Pancreas Reveals Inter- and Intra-cell Population Structure. Cell Syst *3*, 346-360.e4. https://doi.org/10.1016/j.cels.2016.08.011.

Becker, M., Mastropasqua, F., Reising, J.P., Maier, S., Ho, M.-L., Rabkina, I., Li, D., Neufeld, J., Ballenberger, L., Myers, L., et al. (2020). Presynaptic dysfunction in CASK -related

neurodevelopmental disorders. Translational Psychiatry *10*, 1–17. https://doi.org/10.1038/s41398-020-00994-0.

Bölte, S., Willfors, C., Berggren, S., Norberg, J., Poltrago, L., Mevel, K., Coco, C., Fransson, P., Borg, J., Sitnikov, R., et al. (2014). The Roots of Autism and ADHD Twin Study in Sweden (RATSS). Twin Res Hum Genet *17*, 164–176. https://doi.org/10.1017/thg.2014.12.

Bonev, B., Mendelson Cohen, N., Szabo, Q., Fritsch, L., Papadopoulos, G.L., Lubling, Y., Xu, X., Lv, X., Hugnot, J.-P., Tanay, A., et al. (2017). Multiscale 3D Genome Rewiring during Mouse Neural Development. Cell *171*, 557-572.e24. https://doi.org/10.1016/j.cell.2017.09.043.

Brunet, T., Jech, R., Brugger, M., Kovacs, R., Alhaddad, B., Leszinski, G., Riedhammer, K.M., Westphal, D.S., Mahle, I., Mayerhanser, K., et al. (2021). De novo variants in neurodevelopmental disorders—experiences from a tertiary care center. Clinical Genetics *100*, 14–28. https://doi.org/10.1111/cge.13946.

Burke, E.E., Chenoweth, J.G., Shin, J.H., Collado-Torres, L., Kim, S.-K., Micali, N., Wang, Y., Colantuoni, C., Straub, R.E., Hoeppner, D.J., et al. (2020). Dissecting transcriptomic signatures of neuronal differentiation and maturation using iPSCs. Nat Commun *11*, 462. https://doi.org/10.1038/s41467-019-14266-z.

Calzari, L., Barcella, M., Alari, V., Braga, D., Muñoz-Viana, R., Barlassina, C., Finelli, P., Gervasini, C., Barco, A., Russo, S., et al. (2020). Transcriptome Analysis of iPSC-Derived Neurons from Rubinstein-Taybi Patients Reveals Deficits in Neuronal Differentiation. Mol Neurobiol *57*, 3685–3701. https://doi.org/10.1007/s12035-020-01983-6.

Chambers, S.M., Fasano, C.A., Papapetrou, E.P., Tomishima, M., Sadelain, M., and Studer, L. (2009). Highly efficient neural conversion of human ES and iPS cells by dual inhibition of SMAD signaling. Nat Biotechnol *27*, 275–280. https://doi.org/10.1038/nbt.1529.

Connacher, R., Williams, M., Prem, S., Yeung, P.L., Matteson, P., Mehta, M., Markov, A., Peng, C., Zhou, X., McDermott, C.R., et al. (2022). Autism NPCs from both idiopathic and CNV 16p11.2 deletion patients exhibit dysregulation of proliferation and mitogenic responses. Stem Cell Reports *17*, 1380–1394. https://doi.org/10.1016/j.stemcr.2022.04.019.

Connolly, C., Takahashi, S., Miura, H., Hiratani, I., Gilbert, N., Donaldson, A.D., and Hiraga, S.-I. (2022). SAF-A promotes origin licensing and replication fork progression to ensure robust DNA replication. Journal of Cell Science *135*, jcs258991. https://doi.org/10.1242/jcs.258991.

Depienne, C., Nava, C., Keren, B., Heide, S., Rastetter, A., Passemard, S., Chantot-Bastaraud, S., Moutard, M.-L., Agrawal, P.B., VanNoy, G., et al. (2017). Genetic and phenotypic dissection of 1q43q44 microdeletion syndrome and neurodevelopmental phenotypes associated with mutations

in ZBTB18 and HNRNPU. Hum Genet *136*, 463–479. https://doi.org/10.1007/s00439-017-1772-0.

Dugger, S.A., Dhindsa, R.S., De Almeida Sampaio, G., Rafikian, E.E., Petri, S., Letts, V.A., Teoh, J., Ye, J., Colombo, S., Yang, M., et al. (2020). Neurodevelopmental deficits and cell-type-specific transcriptomic perturbations in a mouse model of *HNRNPU* haploinsufficiency. bioRxiv preprint doi: https://doi.org/10.1101/2020.05.01.072512

Durkin, A., Albaba, S., Fry, A.E., Morton, J.E., Douglas, A., Beleza, A., Williams, D., Volker-Touw, C.M.L., Lynch, S.A., Canham, N., et al. (2020). Clinical findings of 21 previously unreported probands with HNRNPU-related syndrome and comprehensive literature review. American Journal of Medical Genetics Part A *182*, 1637–1654. https://doi.org/10.1002/ajmg.a.61599.

Falk, A., Koch, P., Kesavan, J., Takashima, Y., Ladewig, J., Alexander, M., Wiskow, O., Tailor, J., Trotter, M., Pollard, S., et al. (2012). Capture of Neuroepithelial-Like Stem Cells from Pluripotent Stem Cells Provides a Versatile System for In Vitro Production of Human Neurons. PLoS One *7*. https://doi.org/10.1371/journal.pone.0029597.

Fan, H., Lv, P., Huo, X., Wu, J., Wang, Q., Cheng, L., Liu, Y., Tang, Q.-Q., Zhang, L., Zhang, F., et al. (2018). The nuclear matrix protein HNRNPU maintains 3D genome architecture globally in mouse hepatocytes. Genome Res *28*, 192–202. https://doi.org/10.1101/gr.224576.117.

Focșa, I.O., Budișteanu, M., and Bălgrădean, M. (2021). Clinical and genetic heterogeneity of primary ciliopathies (Review). Int J Mol Med *48*, 176. https://doi.org/10.3892/ijmm.2021.5009.

Gandal, M.J., Zhang, P., Hadjimichael, E., Walker, R.L., Chen, C., Liu, S., Won, H., van Bakel, H., Varghese, M., Wang, Y., et al. (2018). Transcriptome-wide isoform-level dysregulation in ASD, schizophrenia, and bipolar disorder. Science *362*, eaat8127. https://doi.org/10.1126/science.aat8127.

Gillentine, M.A., Wang, T., Hoekzema, K., Rosenfeld, J., Liu, P., Guo, H., Kim, C.N., De Vries, B.B.A., Vissers, L.E.L.M., Nordenskjold, M., et al. (2021). Rare deleterious mutations of HNRNP genes result in shared neurodevelopmental disorders. Genome Medicine *13*, 63. https://doi.org/10.1186/s13073-021-00870-6.

Guo, J., Otis, J.M., Suciu, S.K., Catalano, C., Xing, L., Constable, S., Wachten, D., Gupton, S., Lee, J., Lee, A., et al. (2019). Primary Cilia Signaling Promotes Axonal Tract Development and Is Disrupted in Joubert Syndrome-Related Disorders Models. Developmental Cell *51*, 759-774.e5. https://doi.org/10.1016/j.devcel.2019.11.005.

Hu, B., Won, H., Mah, W., Park, R.B., Kassim, B., Spiess, K., Kozlenkov, A., Crowley, C.A., Pochareddy, S., PsychENCODE Consortium, et al. (2021). Neuronal and glial 3D chromatin architecture informs the cellular etiology of brain disorders. Nat Commun *12*, 3968. https://doi.org/10.1038/s41467-021-24243-0.

Huelga, S.C., Vu, A.Q., Arnold, J.D., Liang, T.Y., Liu, P.P., Yan, B.Y., Donohue, J.P., Shiue, L., Hoon, S., Brenner, S., et al. (2012). Integrative genome-wide analysis reveals cooperative regulation of alternative splicing by hnRNP proteins. Cell Rep *1*, 167–178. https://doi.org/10.1016/j.celrep.2012.02.001.

Jones, A.N., Graß, C., Meininger, I., Geerlof, A., Klostermann, M., Zarnack, K., Krappmann, D., and Sattler, M. (2022). Modulation of pre-mRNA structure by hnRNP proteins regulates alternative splicing of MALT1. Science Advances *8*, eabp9153. https://doi.org/10.1126/sciadv.abp9153.

Kiledjian, M., and Dreyfuss, G. (1992). Primary structure and binding activity of the hnRNP U protein: binding RNA through RGG box. EMBO J *11*, 2655–2664. https://doi.org/10.1002/j.1460-2075.1992.tb05331.x.

Kruse, K., Hug, C.B., and Vaquerizas, J.M. (2020). FAN-C: a feature-rich framework for the analysis and visualisation of chromosome conformation capture data. Genome Biology *21*, 303. https://doi.org/10.1186/s13059-020-02215-9.

Liao, Y., Wang, J., Jaehnig, E.J., Shi, Z., and Zhang, B. (2019). WebGestalt 2019: gene set analysis toolkit with revamped UIs and APIs. Nucleic Acids Res *47*, W199–W205. https://doi.org/10.1093/nar/gkz401.

Lieberman-Aiden, E., van Berkum, N.L., Williams, L., Imakaev, M., Ragoczy, T., Telling, A., Amit, I., Lajoie, B.R., Sabo, P.J., Dorschner, M.O., et al. (2009). Comprehensive mapping of long-range interactions reveals folding principles of the human genome. Science *326*, 289–293. https://doi.org/10.1126/science.1181369.

Love, M.I., Huber, W., and Anders, S. (2014). Moderated estimation of fold change and dispersion for RNA-seq data with DESeq2. Genome Biol *15*, 550. https://doi.org/10.1186/s13059-014-0550-8.

Ma, N., Matsunaga, S., Morimoto, A., Sakashita, G., Urano, T., Uchiyama, S., and Fukui, K. (2011). The nuclear scaffold protein SAF-A is required for kinetochore–microtubule attachment and contributes to the targeting of Aurora-A to mitotic spindles. J Cell Sci *124*, 394–404. https://doi.org/10.1242/jcs.063347.

Marchetto, M.C., Belinson, H., Tian, Y., Freitas, B.C., Fu, C., Vadodaria, K.C., Beltrao-Braga, P.C., Trujillo, C.A., Mendes, A.P.D., Padmanabhan, K., et al. (2017). Altered proliferation and

networks in neural cells derived from idiopathic autistic individuals. Mol Psychiatry *22*, 820–835. https://doi.org/10.1038/mp.2016.95.

Marenda, M., Lazarova, E., and Gilbert, N. (2022). The role of SAF-A/hnRNP U in regulating chromatin structure. Current Opinion in Genetics & Development *72*, 38–44. https://doi.org/10.1016/j.gde.2021.10.008.

Merico, D., Isserlin, R., Stueker, O., Emili, A., and Bader, G.D. (2010). Enrichment Map: A Network-Based Method for Gene-Set Enrichment Visualization and Interpretation. PLoS One *5*, e13984. https://doi.org/10.1371/journal.pone.0013984.

Mowat, D., Wilson, M., and Goossens, M. (2003). Mowat-Wilson syndrome. J Med Genet *40*, 305–310. https://doi.org/10.1136/jmg.40.5.305.

Nozawa, R.-S., Boteva, L., Soares, D.C., Naughton, C., Dun, A.R., Buckle, A., Ramsahoye, B., Bruton, P.C., Saleeb, R.S., Arnedo, M., et al. (2017). SAF-A Regulates Interphase Chromosome Structure through Oligomerization with Chromatin-Associated RNAs. Cell *169*, 1214-1227.e18. https://doi.org/10.1016/j.cell.2017.05.029.

Parisian, A.D., Koga, T., Miki, S., Johann, P.D., Kool, M., Crawford, J.R., and Furnari, F.B. (2020). SMARCB1 loss interacts with neuronal differentiation state to block maturation and impact cell stability. Genes Dev *34*, 1316–1329. https://doi.org/10.1101/gad.339978.120.

Paulsen, B., Velasco, S., Kedaigle, A.J., Pigoni, M., Quadrato, G., Deo, A., Adiconis, X., Uzquiano, A., Kim, K., Simmons, S.K., et al. (2020). Human brain organoids reveal accelerated development of cortical neuron classes as a shared feature of autism risk genes. BioRxiv 2020.11.10.376509. https://doi.org/10.1101/2020.11.10.376509.

Pilaz, L.-J., McMahon, J.J., Miller, E.E., Lennox, A.L., Suzuki, A., Salmon, E., and Silver, D.L. (2016). Prolonged Mitosis of Neural Progenitors Alters Cell Fate in the Developing Brain. Neuron *89*, 83–99. https://doi.org/10.1016/j.neuron.2015.12.007.

Poulet, A., Arganda-Carreras, I., Legland, D., Probst, A.V., Andrey, P., and Tatout, C. (2015). NucleusJ: an ImageJ plugin for quantifying 3D images of interphase nuclei. Bioinformatics *31*, 1144–1146. https://doi.org/10.1093/bioinformatics/btu774.

Ramírez, F., Bhardwaj, V., Villaveces, J., Arrigoni, L., Grüning, B.A., Lam, K.C., Habermann, B., Akhtar, A., and Manke, T. (2017). High-resolution TADs reveal DNA sequences underlying genome organization in flies. 115063. https://doi.org/10.1101/115063.

Reimand, J., Isserlin, R., Voisin, V., Kucera, M., Tannus-Lopes, C., Rostamianfar, A., Wadi, L., Meyer, M., Wong, J., Xu, C., et al. (2019). Pathway enrichment analysis and visualization of

omics data using g:Profiler, GSEA, Cytoscape and EnrichmentMap. Nature Protocols *14*, 482–517. https://doi.org/10.1038/s41596-018-0103-9.

Roshon, M.J., and Ruley, H.Earl. (2005). Hypomorphic mutation in hnRNP U results in post-implantation lethality. Transgenic Res *14*, 179–192. https://doi.org/10.1007/s11248-004-8147-8.

Sapir, T., Kshirsagar, A., Gorelik, A., Olender, T., Porat, Z., Scheffer, I.E., Goldstein, D.B., Devinsky, O., and Reiner, O. (2022). Heterogeneous nuclear ribonucleoprotein U (HNRNPU) safeguards the developing mouse cortex. Nat Commun *13*, 4209. https://doi.org/10.1038/s41467-022-31752-z.

Satterstrom, F.K., Kosmicki, J.A., Wang, J., Breen, M.S., De Rubeis, S., An, J.-Y., Peng, M., Collins, R., Grove, J., Klei, L., et al. (2020). Large-Scale Exome Sequencing Study Implicates Both Developmental and Functional Changes in the Neurobiology of Autism. Cell *180*, 568-584.e23. https://doi.org/10.1016/j.cell.2019.12.036.

Shannon, P., Markiel, A., Ozier, O., Baliga, N.S., Wang, J.T., Ramage, D., Amin, N., Schwikowski, B., and Ideker, T. (2003). Cytoscape: a software environment for integrated models of biomolecular interaction networks. Genome Res *13*, 2498–2504. https://doi.org/10.1101/gr.1239303.

Sharp, J.A., Perea-Resa, C., Wang, W., and Blower, M.D. (2020). Cell division requires RNA eviction from condensing chromosomes. Journal of Cell Biology *219*. https://doi.org/10.1083/jcb.201910148.

Stamouli, S., Anderlid, B.-M., Willfors, C., Thiruvahindrapuram, B., Wei, J., Berggren, S., Nordgren, A., Scherer, S.W., Lichtenstein, P., Tammimies, K., et al. (2018). Copy Number Variation Analysis of 100 Twin Pairs Enriched for Neurodevelopmental Disorders. Twin Research and Human Genetics *21*, 1–11. https://doi.org/10.1017/thg.2017.69.

Su, C., Argenziano, M., Lu, S., Pippin, J.A., Pahl, M.C., Leonard, M.E., Cousminer, D.L., Johnson, M.E., Lasconi, C., Wells, A.D., et al. (2021). 3D promoter architecture re-organization during iPSC-derived neuronal cell differentiation implicates target genes for neurodevelopmental disorders. Prog Neurobiol *201*, 102000. https://doi.org/10.1016/j.pneurobio.2021.102000.

Taylor, J., Spiller, M., Ranguin, K., Vitobello, A., Philippe, C., Bruel, A.-L., Cappuccio, G., Brunetti-Pierri, N., Willems, M., Isidor, B., et al. (2022). Expanding the phenotype of HNRNPU-related neurodevelopmental disorder with emphasis on seizure phenotype and review of literature. American Journal of Medical Genetics Part A *n/a*. https://doi.org/10.1002/ajmg.a.62677.

Uhlin, E., Marin Navarro, A., Rönnholm, H., Day, K., Kele, M., and Falk, A. (2017a). Integration Free Derivation of Human Induced Pluripotent Stem Cells Using Laminin 521 Matrix. J Vis Exp 56146. https://doi.org/10.3791/56146.

Uhlin, E., Rönnholm, H., Day, K., Kele, M., Tammimies, K., Bölte, S., and Falk, A. (2017b). Derivation of human iPS cell lines from monozygotic twins in defined and xeno free conditions. Stem Cell Res *18*, 22–25. https://doi.org/10.1016/j.scr.2016.12.006.

Wang, T., Hoekzema, K., Vecchio, D., Wu, H., Sulovari, A., Coe, B.P., Gillentine, M.A., Wilfert, A.B., Perez-Jurado, L.A., Kvarnung, M., et al. (2020). Large-scale targeted sequencing identifies risk genes for neurodevelopmental disorders. Nat Commun *11*. https://doi.org/10.1038/s41467-020-18723-y.

Xiao, R., Tang, P., Yang, B., Huang, J., Zhou, Y., Shao, C., Li, H., Sun, H., Zhang, Y., and Fu, X.-D. (2012). Nuclear Matrix Factor hnRNP U/SAF-A Exerts a Global Control of Alternative Splicing by Regulating U2 snRNP Maturation. Molecular Cell *45*, 656–668. https://doi.org/10.1016/j.molcel.2012.01.009.

Xiong, J., Liu, T., Mi, L., Kuang, H., Xiong, X., Chen, Z., Li, S., and Lin, J.D. (2020). hnRNPU/TrkB Defines a Chromatin Accessibility Checkpoint for Liver Injury and Nonalcoholic Steatohepatitis Pathogenesis. Hepatology *71*, 1228–1246. https://doi.org/10.1002/hep.30921.

Ye, J., Beetz, N., O'Keeffe, S., Tapia, J.C., Macpherson, L., Chen, W.V., Bassel-Duby, R., Olson, E.N., and Maniatis, T. (2015). hnRNP U protein is required for normal pre-mRNA splicing and postnatal heart development and function. Proc Natl Acad Sci USA *112*, E3020–E3029. https://doi.org/10.1073/pnas.1508461112.

Zhang, X., Chen, M.H., Wu, X., Kodani, A., Fan, J., Doan, R., Ozawa, M., Ma, J., Yoshida, N., Reiter, J.F., et al. (2016). Cell-Type-Specific Alternative Splicing Governs Cell Fate in the Developing Cerebral Cortex. Cell *166*, 1147-1162.e15. https://doi.org/10.1016/j.cell.2016.07.025.

Zietzer, A., Hosen, M.R., Wang, H., Goody, P.R., Sylvester, M., Latz, E., Nickenig, G., Werner, N., and Jansen, F. The RNA-binding protein hnRNPU regulates the sorting of microRNA-30c-5p into large extracellular vesicles. J Extracell Vesicles *9*. https://doi.org/10.1080/20013078.2020.1786967.

Zucco, A.J., Dal Pozzo, V., Afinogenova, A., Hart, R.P., Devinsky, O., and Arcangelo, G.D. (2018). Neural progenitors derived from Tuberous Sclerosis Complex patients exhibit attenuated PI3K/AKT signaling and delayed neuronal differentiation. Mol Cell Neurosci *92*, 149–163. https://doi.org/10.1016/j.mcn.2018.08.004.

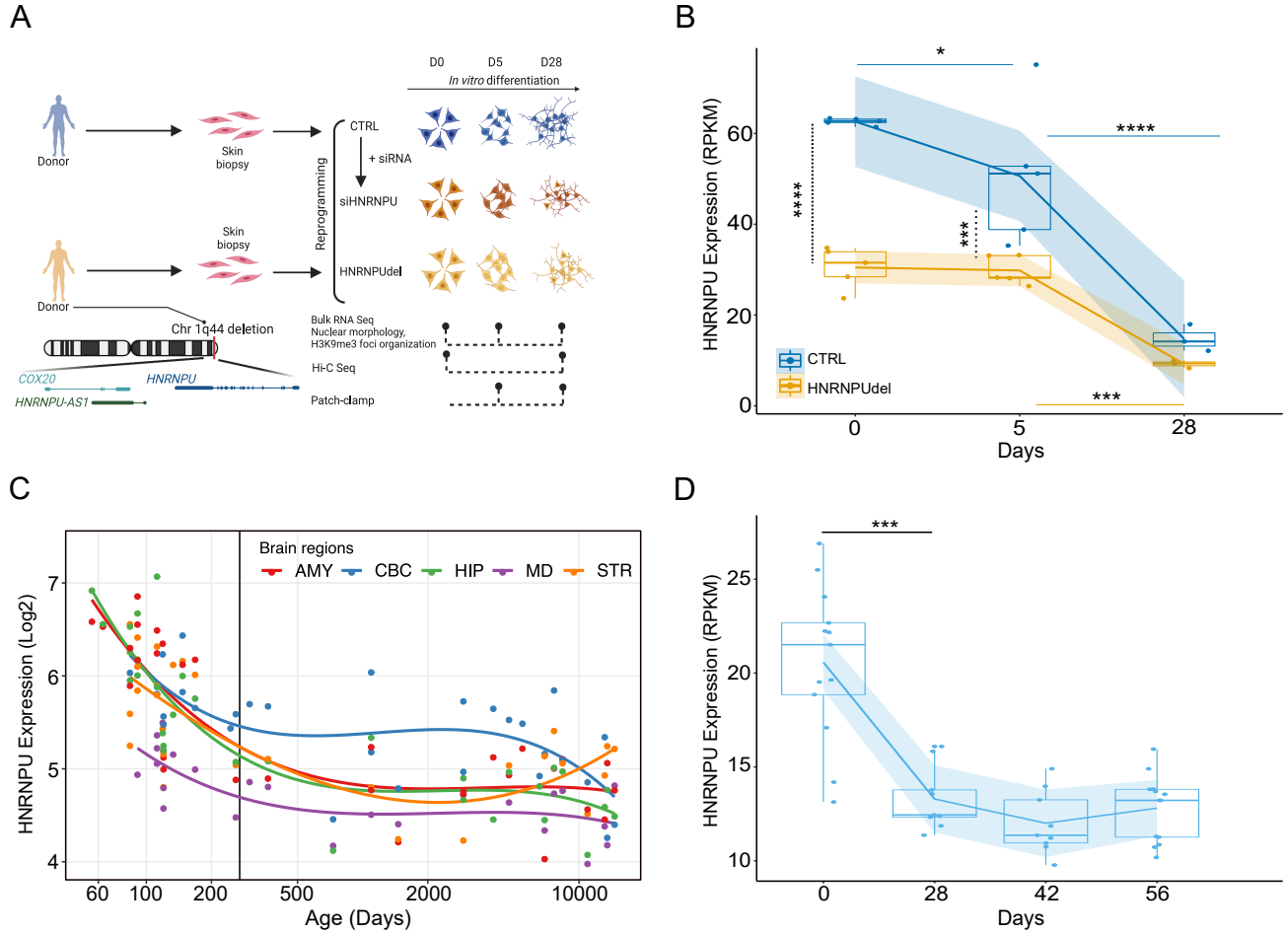
A
D0
D5
D28
In vitro differentiation
Donor
Skin biopsy
CTRL
+ siRNA
siHNRNPU
Reprogramming
Donor
Skin biopsy
HNRNPUdel
Chr 1q44 deletion
COX20
HNRNPU
HNRNPU-AS1
Bulk RNA Seq
Nuclear morphology,
H3K9me3 foci organization
Hi-C Seq
Patch-clamp
B
HNRNPU Expression (RPKM)
Days
CTRL
HNRNPUdel
C
Brain regions
AMY
CBC
HIP
MD
STR
HNRNPU Expression (Log2)
Age (Days)
D
HNRNPU Expression (RPKM)
Days

Figure 1

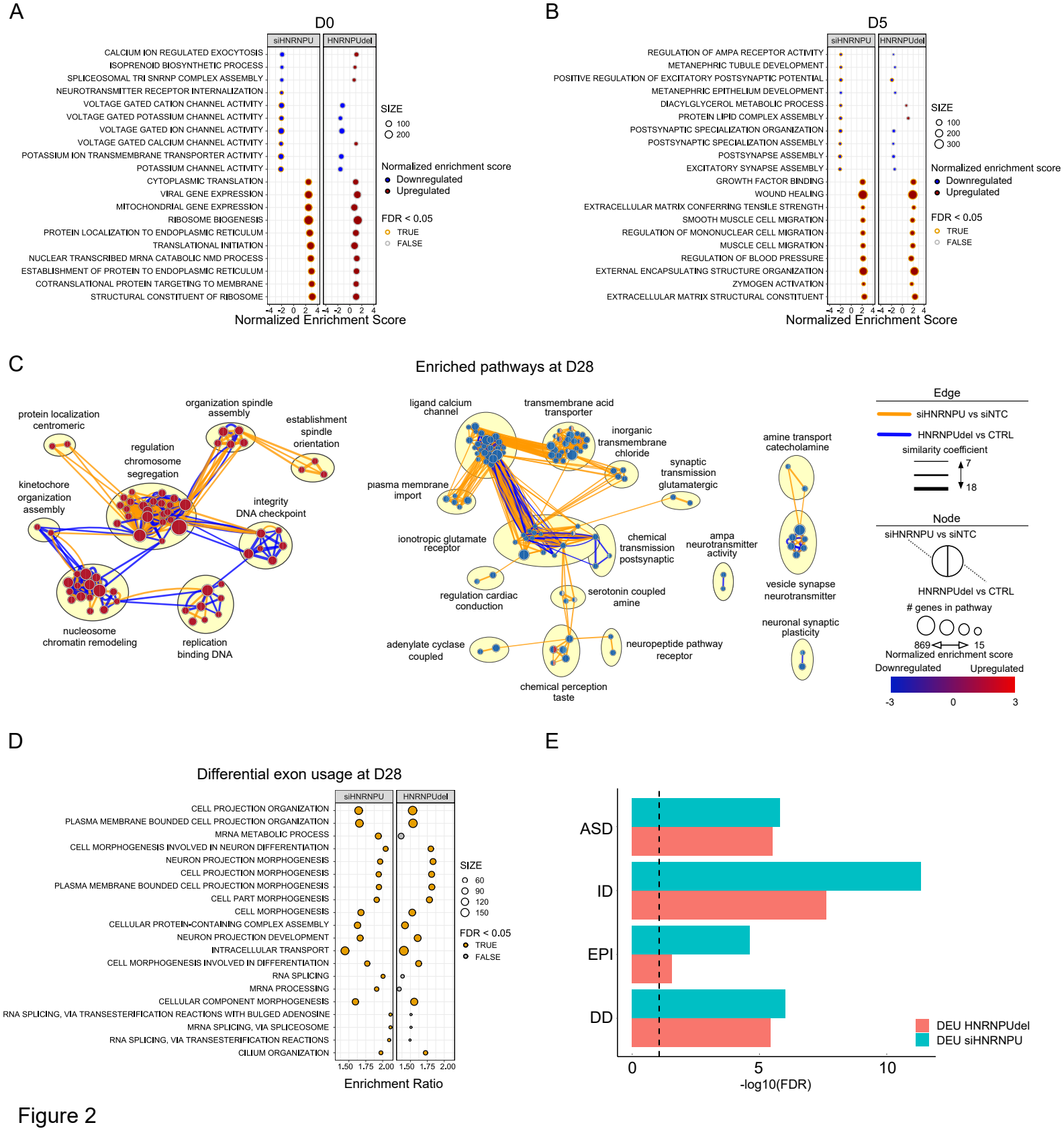
A
D0
siHNRNPU
HNRNPUdel
CALCIUM ION REGULATED EXOCYTOSIS
ISOPRENOID BIOSYNTHETIC PROCESS
SPLICEOSOMAL TRI SNRNP COMPLEX ASSEMBLY
NEUROTRANSMITTER RECEPTOR INTERNALIZATION
VOLTAGE GATED CATION CHANNEL ACTIVITY
VOLTAGE GATED POTASSIUM CHANNEL ACTIVITY
VOLTAGE GATED ION CHANNEL ACTIVITY
VOLTAGE GATED CALCIUM CHANNEL ACTIVITY
POTASSIUM ION TRANSMEMBRANE TRANSPORTER ACTIVITY
POTASSIUM CHANNEL ACTIVITY
CYTOPLASMIC TRANSLATION
VIRAL GENE EXPRESSION
MITOCHONDRIAL GENE EXPRESSION
RIBOSOME BIOGENESIS
PROTEIN LOCALIZATION TO ENDOPLASMIC RETICULUM
TRANSLATIONAL INITIATION
NUCLEAR TRANSCRIBED MRNA CATABOLIC NMD PROCESS
ESTABLISHMENT OF PROTEIN TO ENDOPLASMIC RETICULUM
COTRANSLATIONAL PROTEIN TARGETING TO MEMBRANE
STRUCTURAL CONSTITUENT OF RIBOSOME
-4 -2 0 2 4
Normalized Enrichment Score
SIZE
100
200
Normalized enrichment score
Downregulated
Upregulated
FDR < 0.05
TRUE
FALSE
B
D5
siHNRNPU
HNRNPUdel
REGULATION OF AMPA RECEPTOR ACTIVITY
METANEPHRIC TUBULE DEVELOPMENT
POSITIVE REGULATION OF EXCITATORY POSTSYNAPTIC POTENTIAL
METANEPHRIC EPITHELIUM DEVELOPMENT
DIACYLGLYCEROL METABOLIC PROCESS
PROTEIN LIPID COMPLEX ASSEMBLY
POSTSYNAPTIC SPECIALIZATION ORGANIZATION
POSTSYNAPTIC SPECIALIZATION ASSEMBLY
POSTSYNAPSE ASSEMBLY
EXCITATORY SYNAPSE ASSEMBLY
GROWTH FACTOR BINDING
WOUND HEALING
EXTRACELLULAR MATRIX CONFERRING TENSILE STRENGTH
SMOOTH MUSCLE CELL MIGRATION
REGULATION OF MONONUCLEAR CELL MIGRATION
MUSCLE CELL MIGRATION
REGULATION OF BLOOD PRESSURE
EXTERNAL ENCAPSULATING STRUCTURE ORGANIZATION
ZYMOGEN ACTIVATION
EXTRACELLULAR MATRIX STRUCTURAL CONSTITUENT
-4 -2 0 2 4
Normalized Enrichment Score
SIZE
100
200
300
Normalized enrichment score
Downregulated
Upregulated
FDR < 0.05
TRUE
FALSE
C
Enriched pathways at D28
protein localization centromeric
organization spindle assembly
establishment spindle orientation
regulation chromosome segregation
kinetochore organization assembly
integrity DNA checkpoint
nucleosome chromatin remodeling
replication binding DNA
ligand calcium channel
transmembrane acid transporter
inorganic transmembrane chloride
synaptic transmission glutamatergic
plasma membrane import
ionotropic glutamate receptor
chemical transmission postsynaptic
ampa neurotransmitter activity
regulation cardiac conduction
serotonin coupled amine
adenylate cyclase coupled
neuropeptide pathway receptor
chemical perception taste
amine transport catecholamine
vesicle synapse neurotransmitter
neuronal synaptic plasticity
Edge
siHNRNPU vs siNTC
HNRNPUdel vs CTRL
similarity coefficient
7
18
Node
siHNRNPU vs siNTC
HNRNPUdel vs CTRL
genes in pathway
869
15
Normalized enrichment score
Downregulated
Upregulated
-3
0
3
D
Differential exon usage at D28
siHNRNPU
HNRNPUdel
CELL PROJECTION ORGANIZATION
PLASMA MEMBRANE BOUNDED CELL PROJECTION ORGANIZATION
MRNA METABOLIC PROCESS
CELL MORPHOGENESIS INVOLVED IN NEURON DIFFERENTIATION
NEURON PROJECTION MORPHOGENESIS
CELL PROJECTION MORPHOGENESIS
PLASMA MEMBRANE BOUNDED CELL PROJECTION MORPHOGENESIS
CELL PART MORPHOGENESIS
CELL MORPHOGENESIS
CELLULAR PROTEIN-CONTAINING COMPLEX ASSEMBLY
NEURON PROJECTION DEVELOPMENT
INTRACELLULAR TRANSPORT
CELL MORPHOGENESIS INVOLVED IN DIFFERENTIATION
RNA SPLICING
MRNA PROCESSING
CELLULAR COMPONENT MORPHOGENESIS
RNA SPLICING, VIA TRANSESTERIFICATION REACTIONS WITH BULGED ADENOSINE
MRNA SPLICING, VIA SPLICEOSOME
RNA SPLICING, VIA TRANSESTERIFICATION REACTIONS
CILIUM ORGANIZATION
1.50 1.75 2.00
Enrichment Ratio
SIZE
60
90
120
150
FDR < 0.05
TRUE
FALSE
E
ASD
ID
EPI
DD
0
5
10
-log10(FDR)
DEU HNRNPUdel
DEU siHNRNPU

Figure 2

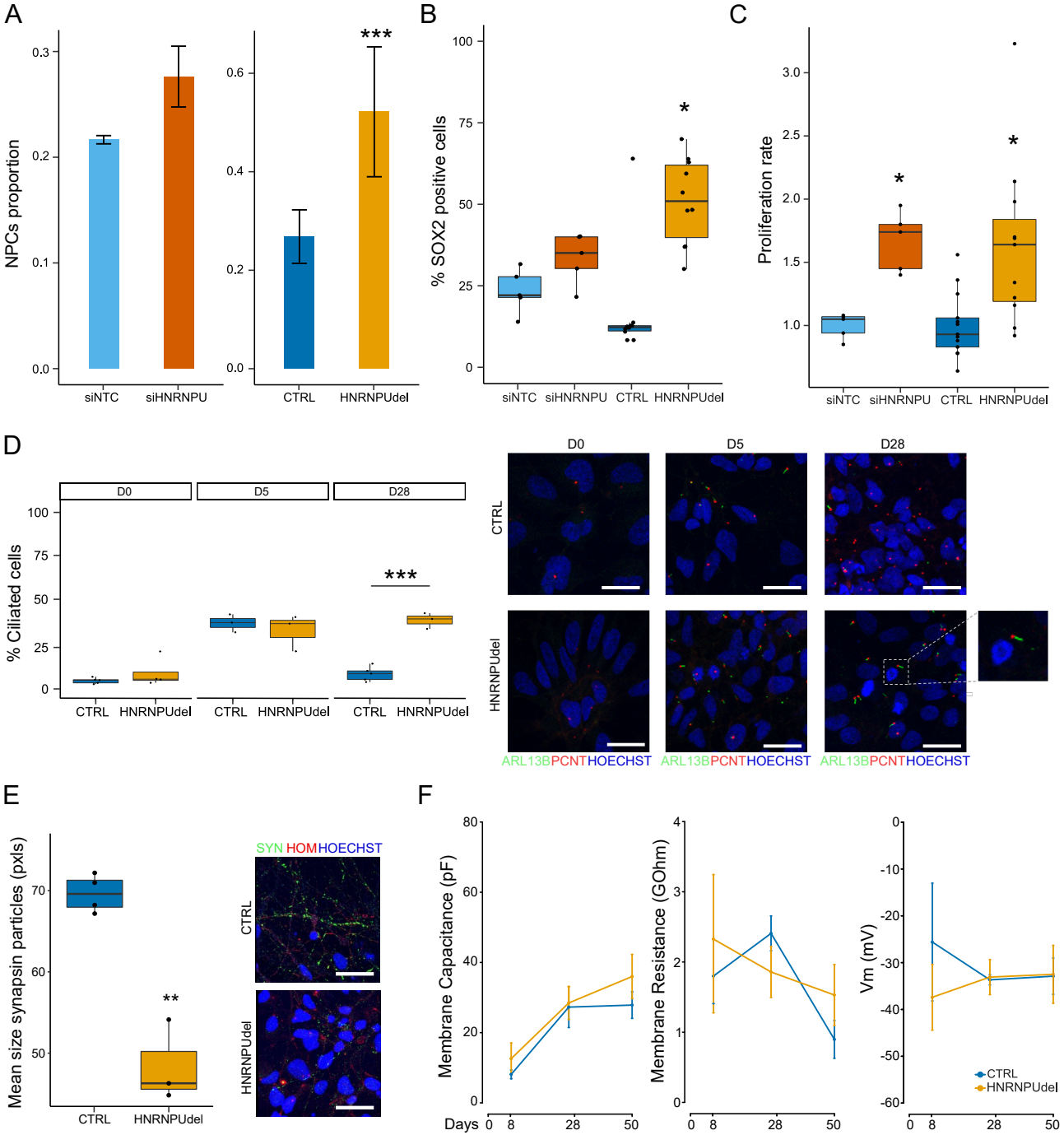
A
NPCs proportion
0.0
0.1
0.2
0.3
siNTC
siHNRNPU
0.0
0.2
0.4
0.6
***
CTRL
HNRNPUdel
B
% SOX2 positive cells
0
25
50
75
100
*
siNTC
siHNRNPU
CTRL
HNRNPUdel
C
Proliferation rate
1.0
1.5
2.0
2.5
3.0
*
*
siNTC
siHNRNPU
CTRL
HNRNPUdel
D
% Ciliated cells
D0
D5
D28
0
25
50
75
100
***
CTRL
HNRNPUdel
CTRL
HNRNPUdel
CTRL
HNRNPUdel
D0
D5
D28
CTRL
HNRNPUdel
ARL13B PCNT HOECHST
ARL13B PCNT HOECHST
ARL13B PCNT HOECHST
E
Mean size synapsin particles (pxls)
50
60
70
**
CTRL
HNRNPUdel
SYN HOM HOECHST
CTRL
HNRNPUdel
F
Membrane Capacitance (pF)
0
20
40
60
80
Days
0
8
28
50
Membrane Resistance (GOhm)
0
1
2
3
4
0
8
28
50
Vm (mV)
0
-10
-20
-30
-40
-50
-60
0
8
28
50
CTRL
HNRNPUdel

Figure 3

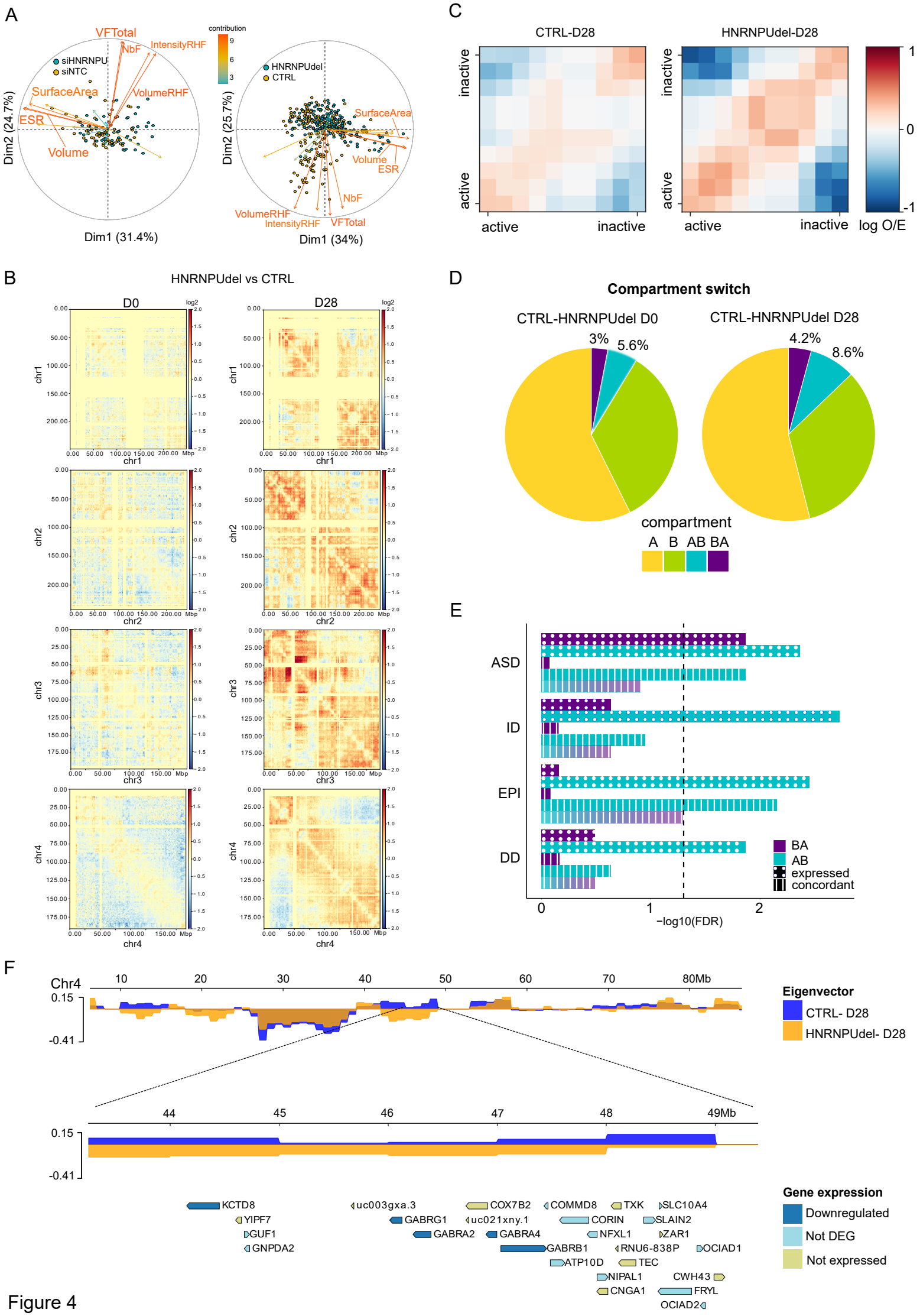
A
VFTotal
NbF
IntensityRHF
siHNRNPU
siNTC
SurfaceArea
VolumeRHF
ESR
Volume
Dim2 (24.7%)
Dim1 (31.4%)
contribution
9
6
3
HNRNPUdel
CTRL
SurfaceArea
Volume
ESR
NbF
VolumeRHF
IntensityRHF
VFTotal
Dim2 (25.7%)
Dim1 (34%)
C
CTRL-D28
HNRNPUdel-D28
inactive
active
log O/E
B
HNRNPUdel vs CTRL
D0
D28
log2
chr1
chr2
chr3
chr4
Mbp
D
Compartment switch
CTRL-HNRNPUdel D0
CTRL-HNRNPUdel D28
3%
5.6%
4.2%
8.6%
compartment
A B AB BA
E
ASD
ID
EPI
DD
BA
AB
expressed
concordant
−log10(FDR)
F
Chr4
Mbp
Eigenvector
CTRL- D28
HNRNPUdel- D28
Gene expression
Downregulated
Not DEG
Not expressed
KCTD8
uc003gxa.3
COX7B2
COMMD8
TXK
SLC10A4
YIPF7
GABRG1
uc021xny.1
CORIN
SLAIN2
GUF1
GABRA2
GABRA4
NFXL1
ZAR1
GNPDA2
GABRB1
RNU6-838P
OCIAD1
ATP10D
TEC
NIPAL1
CWH43
CNGA1
FRYL
OCIAD2

Figure 4

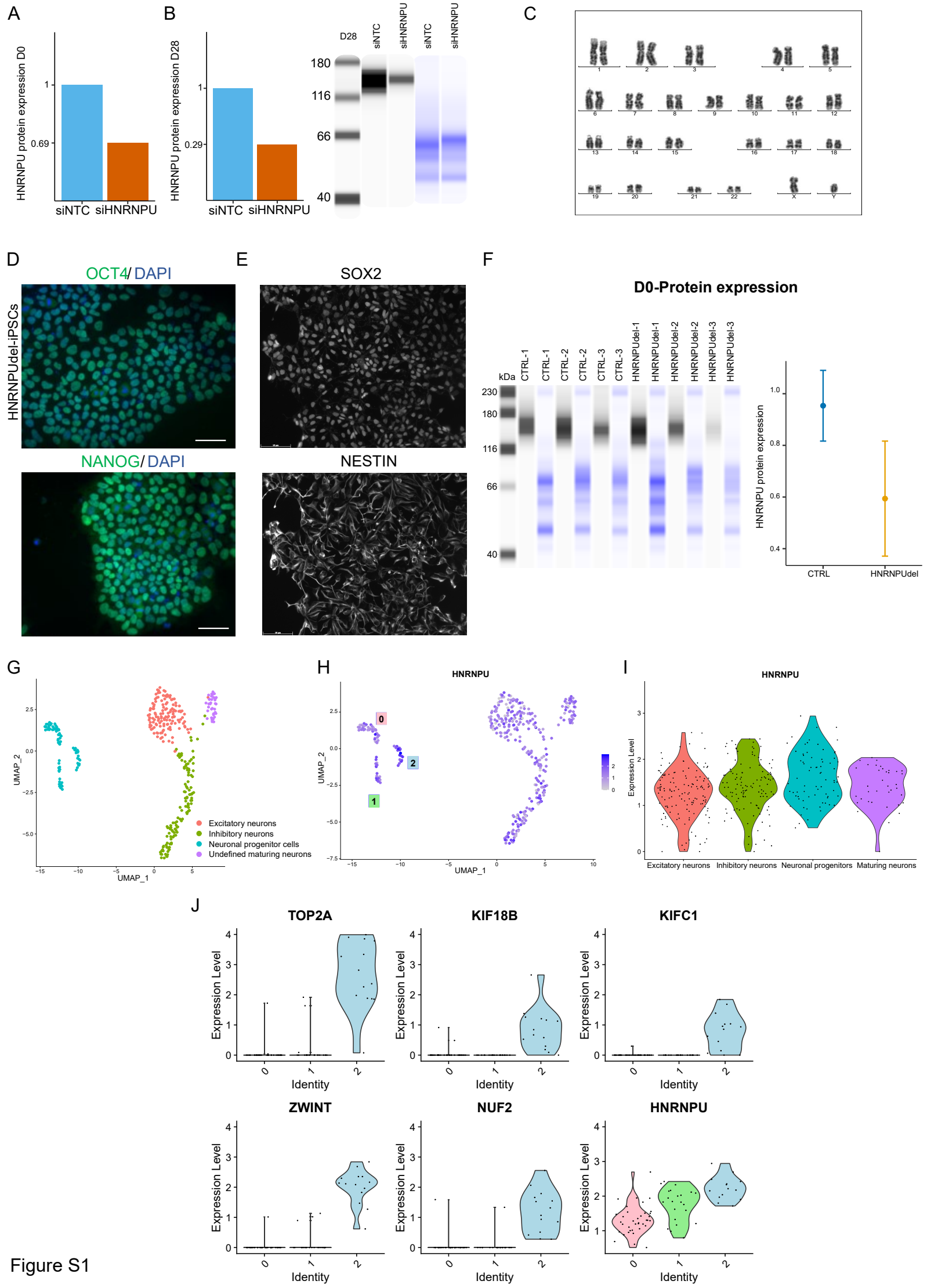
A
HNRNPU protein expression D0
1
0.69
siNTC
siHNRNPU
B
HNRNPU protein expression D28
1
0.29
siNTC
siHNRNPU
D28
siNTC
siHNRNPU
siNTC
siHNRNPU
180
116
66
40
C
D
OCT4/ DAPI
HNRNPUdel-iPSCs
NANOG/ DAPI
E
SOX2
NESTIN
F
D0-Protein expression
kDa
CTRL-1
CTRL-1
CTRL-2
CTRL-2
CTRL-3
CTRL-3
HNRNPUdel-1
HNRNPUdel-1
HNRNPUdel-2
HNRNPUdel-2
HNRNPUdel-3
HNRNPUdel-3
230
180
116
66
40
HNRNPU protein expression
1.0
0.8
0.6
0.4
CTRL
HNRNPUdel
G
UMAP_2
UMAP_1
Excitatory neurons
Inhibitory neurons
Neuronal progenitor cells
Undefined maturing neurons
H
HNRNPU
0
1
2
UMAP_2
UMAP_1
I
HNRNPU
Expression Level
Excitatory neurons
Inhibitory neurons
Neuronal progenitors
Maturing neurons
J
TOP2A
KIF18B
KIFC1
ZWINT
NUF2
HNRNPU
Expression Level
Identity

Figure S1

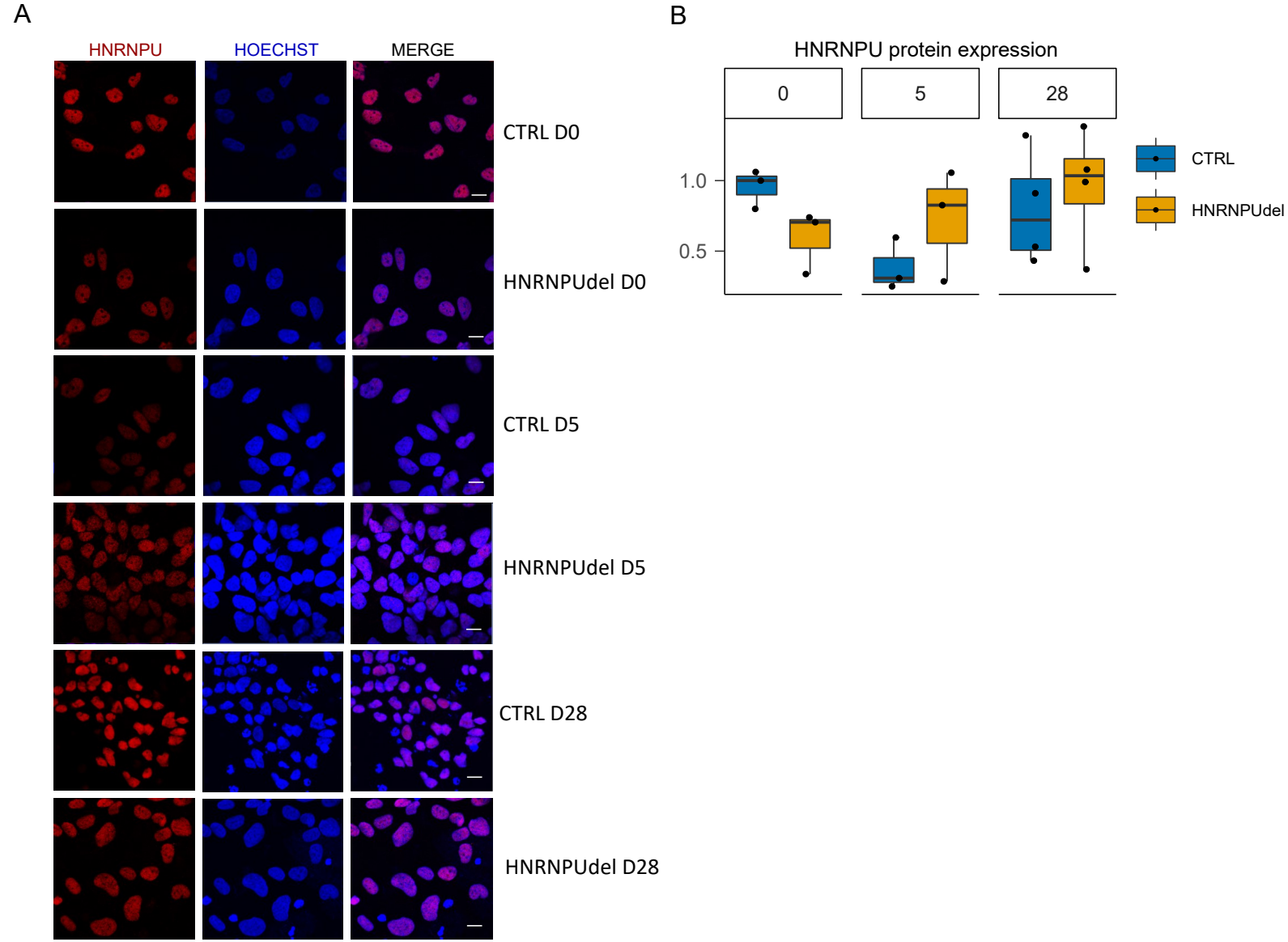
A
HNRNPU
HOECHST
MERGE
CTRL D0
HNRNPUdel D0
CTRL D5
HNRNPUdel D5
CTRL D28
HNRNPUdel D28
B
HNRNPU protein expression
0
5
28
1.0
0.5
CTRL
HNRNPUdel

Figure S2

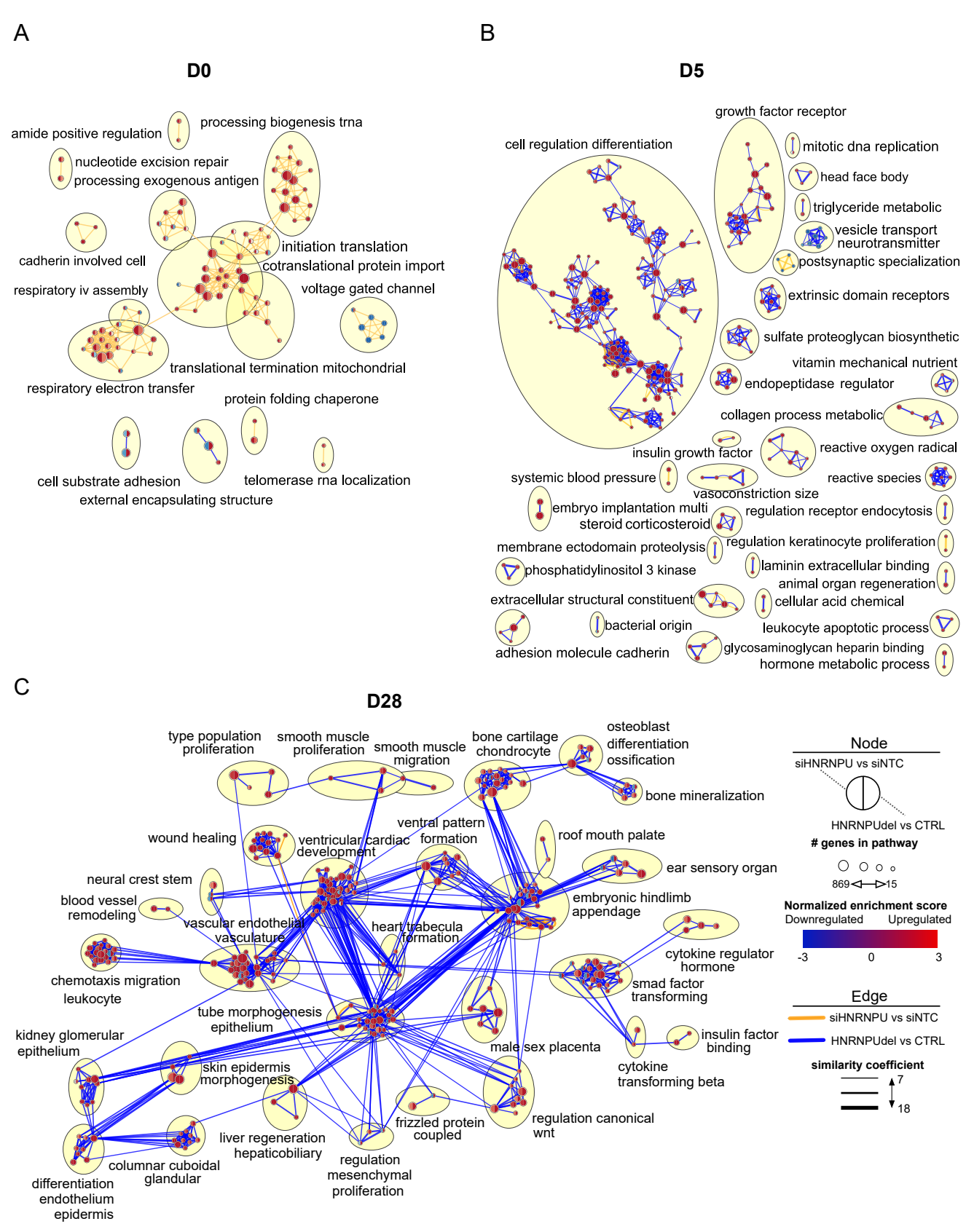
A
D0
amide positive regulation
processing biogenesis trna
nucleotide excision repair
processing exogenous antigen
cadherin involved cell
initiation translation
cotranslational protein import
respiratory iv assembly
voltage gated channel
translational termination mitochondrial
respiratory electron transfer
protein folding chaperone
cell substrate adhesion
telomerase rna localization
external encapsulating structure
B
D5
growth factor receptor
cell regulation differentiation
mitotic dna replication
head face body
triglyceride metabolic
vesicle transport
neurotransmitter
postsynaptic specialization
extrinsic domain receptors
sulfate proteoglycan biosynthetic
vitamin mechanical nutrient
endopeptidase regulator
collagen process metabolic
insulin growth factor
reactive oxygen radical
systemic blood pressure
reactive species
vasoconstriction size
embryo implantation multi
regulation receptor endocytosis
steroid corticosteroid
membrane ectodomain proteolysis
regulation keratinocyte proliferation
phosphatidylinositol 3 kinase
laminin extracellular binding
animal organ regeneration
extracellular structural constituent
cellular acid chemical
bacterial origin
leukocyte apoptotic process
adhesion molecule cadherin
glycosaminoglycan heparin binding
hormone metabolic process
C
D28
type population proliferation
smooth muscle proliferation
smooth muscle migration
bone cartilage chondrocyte
osteoblast differentiation ossification
bone mineralization
wound healing
ventricular cardiac development
ventral pattern formation
roof mouth palate
ear sensory organ
neural crest stem
blood vessel remodeling
vascular endothelial vasculature
heart trabecula formation
embryonic hindlimb appendage
cytokine regulator hormone
chemotaxis migration leukocyte
smad factor transforming
tube morphogenesis epithelium
kidney glomerular epithelium
male sex placenta
insulin factor binding
skin epidermis morphogenesis
cytokine transforming beta
frizzled protein coupled
regulation canonical wnt
liver regeneration hepaticobiliary
columnar cuboidal glandular
regulation mesenchymal proliferation
differentiation endothelium epidermis
Node
siHNRNPU vs siNTC
HNRNPUdel vs CTRL
genes in pathway
869
15
Normalized enrichment score
Downregulated
Upregulated
-3
0
3
Edge
siHNRNPU vs siNTC
HNRNPUdel vs CTRL
similarity coefficient
7
18
D
siHNRNPU D0
siHNRNPU D5
siHNRNPU D28
HNRNPUdel D0
HNRNPUdel D5
HNRNPUdel D28
-log10(padj)
log2FoldChange

Figure S3

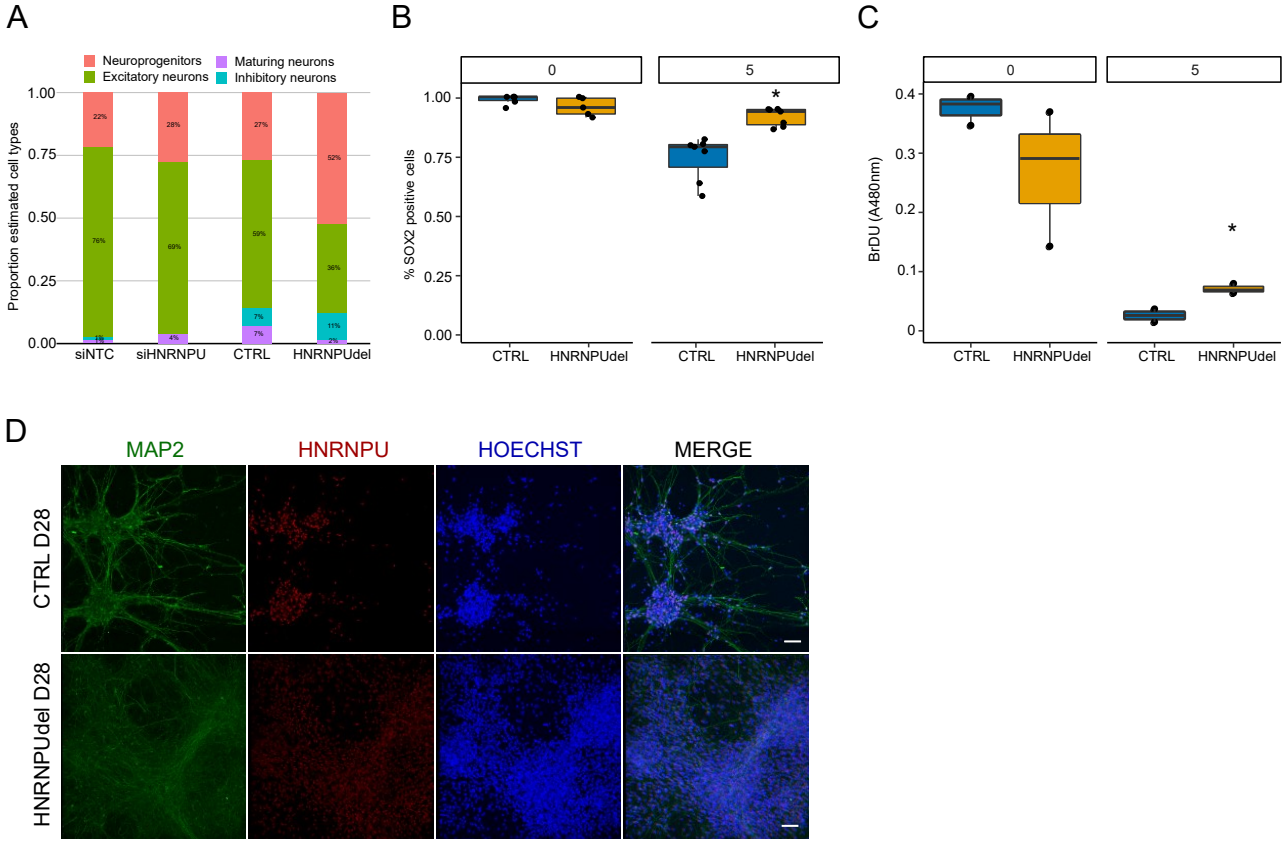
A
Neuroprogenitors
Excitatory neurons
Maturing neurons
Inhibitory neurons
Proportion estimated cell types
1.00
0.75
0.50
0.25
0.00
22%
76%
1%
28%
69%
4%
27%
59%
7%
7%
52%
36%
11%
2%
siNTC
siHNRNPU
CTRL
HNRNPUdel
B
0
5
% SOX2 positive cells
1.00
0.75
0.50
0.25
0.00
*
CTRL
HNRNPUdel
CTRL
HNRNPUdel
C
0
5
BrDU (A480nm)
0.4
0.3
0.2
0.1
0
*
CTRL
HNRNPUdel
CTRL
HNRNPUdel
D
MAP2
HNRNPU
HOECHST
MERGE
CTRL D28
HNRNPUdel D28

Figure S4

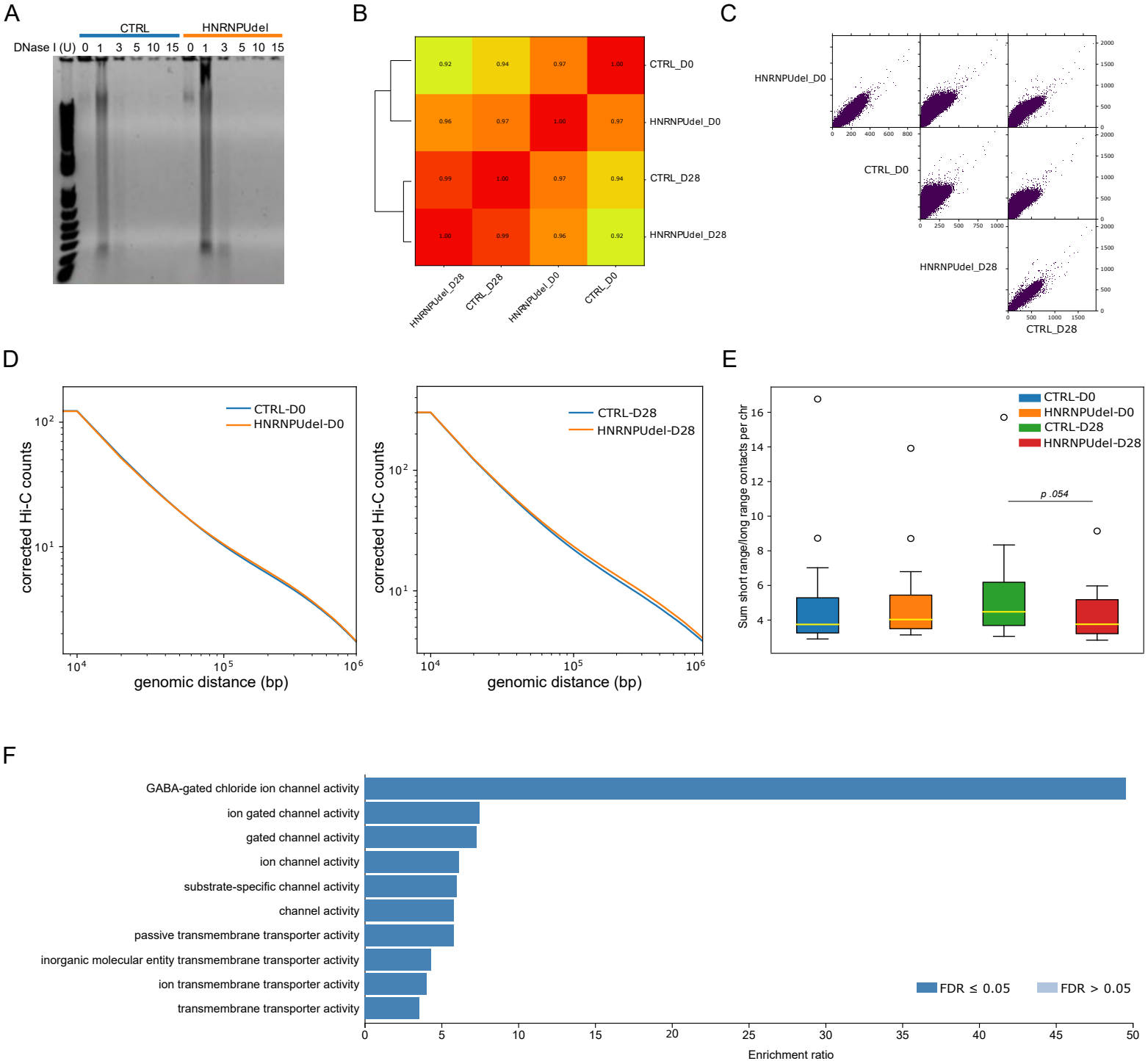
A
CTRL
HNRNPUdel
DNase I (U) 0 1 3 5 10 15 0 1 3 5 10 15
B
CTRL_D0
HNRNPUdel_D0
CTRL_D28
HNRNPUdel_D28
C
HNRNPUdel_D0
CTRL_D0
HNRNPUdel_D28
CTRL_D28
D
CTRL-D0
HNRNPUdel-D0
CTRL-D28
HNRNPUdel-D28
corrected Hi-C counts
genomic distance (bp)
E
CTRL-D0
HNRNPUdel-D0
CTRL-D28
HNRNPUdel-D28
p .054
Sum short range/long range contacts per chr
F
GABA-gated chloride ion channel activity
ion gated channel activity
gated channel activity
ion channel activity
substrate-specific channel activity
channel activity
passive transmembrane transporter activity
inorganic molecular entity transmembrane transporter activity
ion transmembrane transporter activity
transmembrane transporter activity
FDR ≤ 0.05
FDR > 0.05
Enrichment ratio

Figure S5